



Attribution–NonCommercial–NoDerivs 2.0 KOREA

You are free to :

- **Share** — copy and redistribute the material in any medium or format

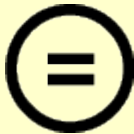
Under the following terms :



Attribution — You must give [appropriate credit](#), provide a link to the license, and [indicate if changes were made](#). You may do so in any reasonable manner, but not in any way that suggests the licensor endorses you or your use.




NonCommercial — You may not use the material for [commercial purposes](#).



NoDerivatives — If you [remix, transform, or build upon](#) the material, you may not distribute the modified material.

You do not have to comply with the license for elements of the material in the public domain or where your use is permitted by an applicable exception or limitation.

This is a human-readable summary of (and not a substitute for) the [license](#).

[Disclaimer](#) 

Improved Image Quality Using Joint Image
Reconstruction and Non-Local Means
Filtering for Multi-Spectral SPECT

Minh Phuong Nguyen

Department of Electrical and Computer Engineering

Graduate School of UNIST

2016

Improved Image Quality Using Joint Image
Reconstruction and Non-Local Means
Filtering for Multi-Spectral SPECT

Minh Phuong Nguyen

Department of Electrical and Computer Engineering

Graduate School of UNIST

Improved Image Quality Using Joint Image
Reconstruction and Non-Local Means
Filtering for Multi-Spectral SPECT

A thesis
submitted to the Graduate School of UNIST
in partial fulfillment of the
requirements for the degree of
Master of Science

Minh Phuong Nguyen

07 June 2016

Approved by



Advisor

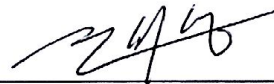
Se Young Chun

Improved Image Quality Using Joint Image
Reconstruction and Non-Local Means
Filtering for Multi-Spectral SPECT

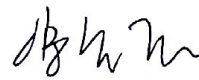
Minh Phuong Nguyen

This certifies that the thesis of
Minh Phuong Nguyen is approved.

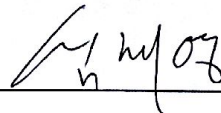
07 June 2016



Advisor: Se Young Chun



Seungjoon Yang: Thesis Committee Member #1



Jae-Young Sim: Thesis Committee Member #2

Abstract

Single photon emission computed tomography (SPECT) is one of the major imaging modalities in medical imaging, including quantitative imaging for the evaluation of efficacy and toxicity in radionuclide therapy. Choosing optimal SPECT image reconstruction strategy for radionuclides with wide energy spectrum affects resulting image quality due to energy-dependent attenuation information in forward projection models and energy-dependent scatter information. A post-reconstruction filtering is also important to suppress noise propagated during reconstruction process.

Yttrium-90 (Y-90) is a commonly used radionuclide in targeted radionuclide therapy. Recently, bremsstrahlung in Y-90 has been successfully imaged for good quantification of radioactivity to predict therapy response more accurately. However, wide continuous energy spectrum of bremsstrahlung photons is challenging in Y-90 SPECT image reconstruction. Previously, forward projection models with narrow single-energy window were used for image reconstruction from a single acquisition energy window. We propose a new Y-90 SPECT joint image reconstruction method from multiple acquisitions windows, referred to as joint spectral reconstruction (JSR) using multi-energy window forward models. Our proposed method yielded significantly higher recovery coefficient and lower standard deviation than other methods that use a single acquisition window and single energy window for projection model with narrow and wide energy spectra.

We also investigated parameter selection methods for non-local mean (NLM) filter with SPECT. Self-weight estimation is an important factor to influence denoising performance of NLM. Recently introduced local James-Stein type center pixel weight method (LJS) outperformed other existing self-weight estimation methods in determining the contribution of the self-weight to NLM. However, the LJS method may result in excessively large self-weight estimates since no upper bound for self-weights was assumed. It also used relatively large local area for estimating self-weights, which may lead to strong bias. We propose novel local minimax self-weight estimation

methods with direct bounds (LMM-DB) and re-parametrization (LMM-RP) using Baranchik's minimax estimator. Our proposed methods yielded better bias-variance trade-off, higher peak signal-to-noise (PSNR) ratio, and less visual artifacts than the classical NLM method and the original LJS method. Our proposed methods also provide a heuristic way of choosing global smoothing parameters of NLM to yield PSNR values that are close to the optimal values without knowing the true image.

Contents

Contents	iii
List of Figures	iv
I. Introduction	1
1.1 Fundamental Background	1
1.1.1 Basic Principle of SPECT	1
1.1.2 Multi-spectral SPECT	3
1.1.3 Post-reconstruction Filtering	5
1.2 Contribution of This Thesis	7
1.3 Organization of This Thesis	7
II. Joint Spectral Image Reconstruction for Y-90 SPECT	8
2.1 Related Works	8
2.2 Methods	9
2.3 Results	11
2.3.1 Results for Narrow Windows	11
2.3.2 Results for Wide Windows	11
2.4 Discussion	12
III. Post-reconstruction Non-local Means Filtering	16
3.1 Related Works	16
3.2 Review on Local James-Stein Self-Weight Estimation for Non Local Means Filter	17
3.2.1 Reviewing Classical Non-Local Means Filter	17
3.2.2 Reviewing Local James-Stein Self-Weight Estimation	18
3.3 Limitations of Local James-Stein Self-Weight Estimation for Non Local Means Filter	19
3.3.1 Size of Local Neighborhood for Self-Weight Estimation	19
3.3.2 Excessively Large Self-Weight Estimation	20

3.4	Local Minimax Estimation Methods for Upper Bounded Self-Weights in Non Local Means Filter	22
3.4.1	Bounded Self-Weights	22
3.4.2	Local Minimax Self-Weight Estimation with Direct Bound	23
3.4.3	Local Minimax Self-Weight Estimation with Reparametrization	25
3.5	Simulation Results	27
3.5.1	Simulation Setup	27
3.5.2	Performance Studies with PSNR	28
3.5.3	Performance Studies with Bias-Variance Trade-Off	28
3.5.4	Performance Studies with Visual Quality Assessment	29
3.5.5	Maximum Self-Weights: One vs. Stein's	30
3.5.6	"Practical" Minimax Estimator	30
3.6	Discussion	31
IV.	Conclusion	38
	References	39

List of Figures

1.1	Iterative image reconstruction.	2
1.2	Illustration of gamma decay through multiple energy states.	3
1.3	Energy spectra of some radionuclides used in internal radiotherapy, generated using SIMIND Monte Carlo simulation. This figure is published in [1], reprinted with permission of authors and the Society of Nuclear Medicine and Molecular Imaging, Inc.	4
1.4	Reference and reconstructed image at different iteration number of a Y-90 SPECT.	5
2.1	MC simulated and fitted CDR using Gaussian/B-spline (all in log scale).	13
2.2	RC, SD, and Bias for narrow window case (LEFT) and wide window case (RIGHT).	14
2.3	True and reconstructed images at 35 iteration for narrow and wide window cases.	15

LIST OF FIGURES

3.1	Bias-variance curves (cameraman example) for the classical NLM and the LJS method (LJS ₊) for different sizes of local neighborhood (B). The curves are plotted with varying the smoothing parameter h ($\log_2 h \in [1.8, 3.2]$).	19
3.2	Denoised image of cameraman example using the original LJS method [2] with no upper bound for self-weights (top left), estimated p_i values (top right), calculated W_i 's (bottom left), and resulting self-weights ($w_{i,i}$) showing excessive self-weights (bottom right). $B = 2$ and $\sigma = 10$	21
3.3	Graphical illustrations of the original and positive part JS estimators without upper bounds and the proposed minimax self-weight estimators with upper bounds in terms of $c(\ \mathbf{s}\)$ vs. $\ \mathbf{s}\ $	24
3.4	Bias-variance curves for natural images using LJS ₊ [2] and our proposed LMM – DB ^{one} , LMM – RP ^{one} methods with a noise level $\sigma = 10$	29
3.5	Cameraman: True, noisy ($\sigma = 10$), and filtered images using LJS ₊ [2], proposed LMM – DB ^{one} , and LMM – RP ^{one}	32
3.6	SPECT: True, noisy ($\sigma = 3$), and filtered images using LJS ₊ [2], proposed LMM – DB ^{one} , and LMM – RP ^{one}	33
3.7	Filtered results for various natural images using LJS ₊ [2] and proposed LJS – RP ^{one} with noise level $\sigma = 10$ and neighborhood size $B = 2$	34
3.8	Bias-variance curves and PSNR over varying neighborhood size (B) using classical NLM (only in PSNR figure), LJS, and proposed LMM – DB ^{stein} vs. LMM – DB ^{one} for cameraman example.	35
3.9	Comparison plots of RMSE vs. smoothing parameter h and the percentage of $c(\ \mathbf{s}\) > 2$ vs. the same smoothing parameter when using LMM-DB and LMM-RP with $B = 2$. $\sigma = 10$ for cameraman and $\sigma = 3$ for SPECT.	36

Introduction

1.1 Fundamental Background

1.1.1 Basic Principle of SPECT

Single photon emission computed tomography (SPECT) employs the principal of computed tomography in imaging the radionuclides (also called *tracer*, or *radiotracer*) that emit single gamma (γ) rays. Gamma rays are produced when an nuclei in excited state (X^*) decays to a more stable state (Y^*) by rearrange its protons and neutrons without altering its mass number A and atomic number Z (refer to I.1). Gamma rays are emitted from various radioactive sources and often follow other nuclear decay processes such as beta decay or alpha decay. Gamma rays are electromagnetic waves having very high-frequency and short wavelength so that they are able to pass through body and can be used for medical imaging. SPECT can also image some other kinds of radiation such as bremsstrahlung which is generated from Y-90 radionuclide. In the following parts of this introduction, we only refer to γ radiation, but the same principle can also be applied to other kinds of radiation used in SPECT.



The emitted γ rays are imaged by a special camera (also called *detector*), commonly consists of NaI(Tl) scintillator or CZT semiconductor. The detector generates light photons when radi-

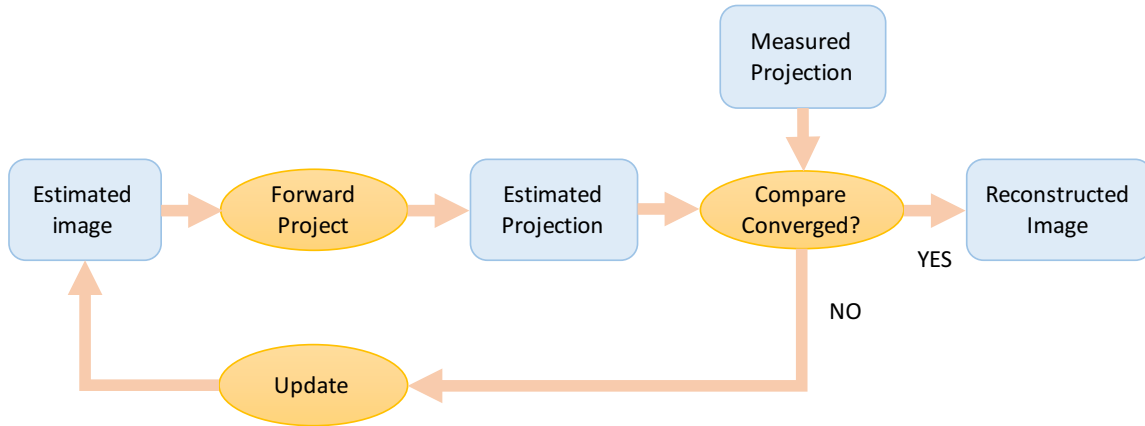


Figure 1.1: Iterative image reconstruction.

ated rays interact with its surface. Light is converted to electric signals by photomultiplier tubes attached to the detector. Then positions and energy of the photons can be digitalized and processed to form images. At a specific angle, the detector camera can record only two-dimensional (2D) projections of the three-dimensional (3D) radiation distribution. This is sufficient for some applications such as bone imaging. However, in many cases the lack of depth information hinder adequate localization of the interested radiation area. SPECT uses rotating cameras to obtain multiple projections (called *sinogram*) from different angles around the subject and utilizes mathematical algorithms to reconstruct 3D images of the distribution. While a single rotating camera can capture the whole 3D area, using dual-camera or triple-camera detector helps improving image quality as well as reducing acquisition time.

Reconstructing image from its projections can be effectively done using iterative method (*iterative reconstruction*). The basic principal is illustrated in Fig. 1.1. Starting from an image's initial estimate, which usually has all zero or all one pixel intensities, projection profiles are calculated using a forward projection model. This projection data is then compared with the real measured projection data so that the algorithm can decide how to update a closer estimate of the image. The algorithm iterates several times until an acceptably small error between the calculated projections and measured projections is reached. A part of γ rays emitted from radionuclide source may not reach the detector straightly, but be attenuated or scattered when the γ photons collide with matters in the medium prior to detection. The γ photons also have some interaction with collimators on the detector which affect image quality. All these factors should be considered in image reconstruction process.

Since iterative reconstruction requires to run several iterations and incorporate complex modelling of the mentioned aspects of imaging devices, it is computationally expensive. However with the development of computer processors and programming algorithms, iterative recon-

struction is increasingly used in computed tomography. A popular algorithm used to accelerate the reconstruction is called *ordered subsets* in which only a small number (or *subset*) of projection angles spaced regularly is used in each iteration. For example, 60 views $\{x_i\}, i = 0, \dots, 59$ captured at every 6° while camera rotates 360° around the subject can be splitted into 6 subsets $\{x_{k+6i}\}, i = 0, \dots, 9$ for $k = 0, \dots, 5$. This algorithm assumes that for each iteration of reconstruction, using only a subset of projections can give as good image estimate as using all projections.

1.1.2 Multi-spectral SPECT

An excited state of a nuclei may decay into multiple less excited states and these less excited states can either remain their energy or decay more until reaching the ground state (Fig. 1.2). Each decay from one state to another emit a γ ray of an energy proportional to energy difference between the two states. Some states have higher probability of decay events than the others. Besides, some photons undergo scatter and attenuation within the subject and loose some energy before arriving at the detector. Consequently, detected γ rays spread over an energy spectrum that has range and peaks depending on the characteristic of particular radionuclide.

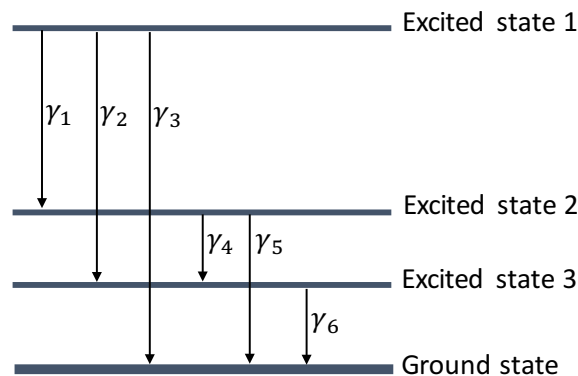


Figure 1.2: Illustration of gamma decay through multiple energy states.

Only photons that have straight emission trajectory are interested for imaging because they represent correctly positions of radiation particles. These photons are called primary photons. Photons that are deviated from their initial trajectory under some interactions with medium, mostly related to scatter, are undesired and should be excluded during reconstruction. Available techniques are able to use mathematical models or simulation codes to estimate these undesired photons and subtract them from total measurement to obtain the primary. Fig. 1.3 presents energy spectra of some radionuclides used in internal radiotherapy.

It is important to select appropriate acquisition windows and scatter windows. Exact location and width of the window should be optimized using simulation and phantom experiments. When

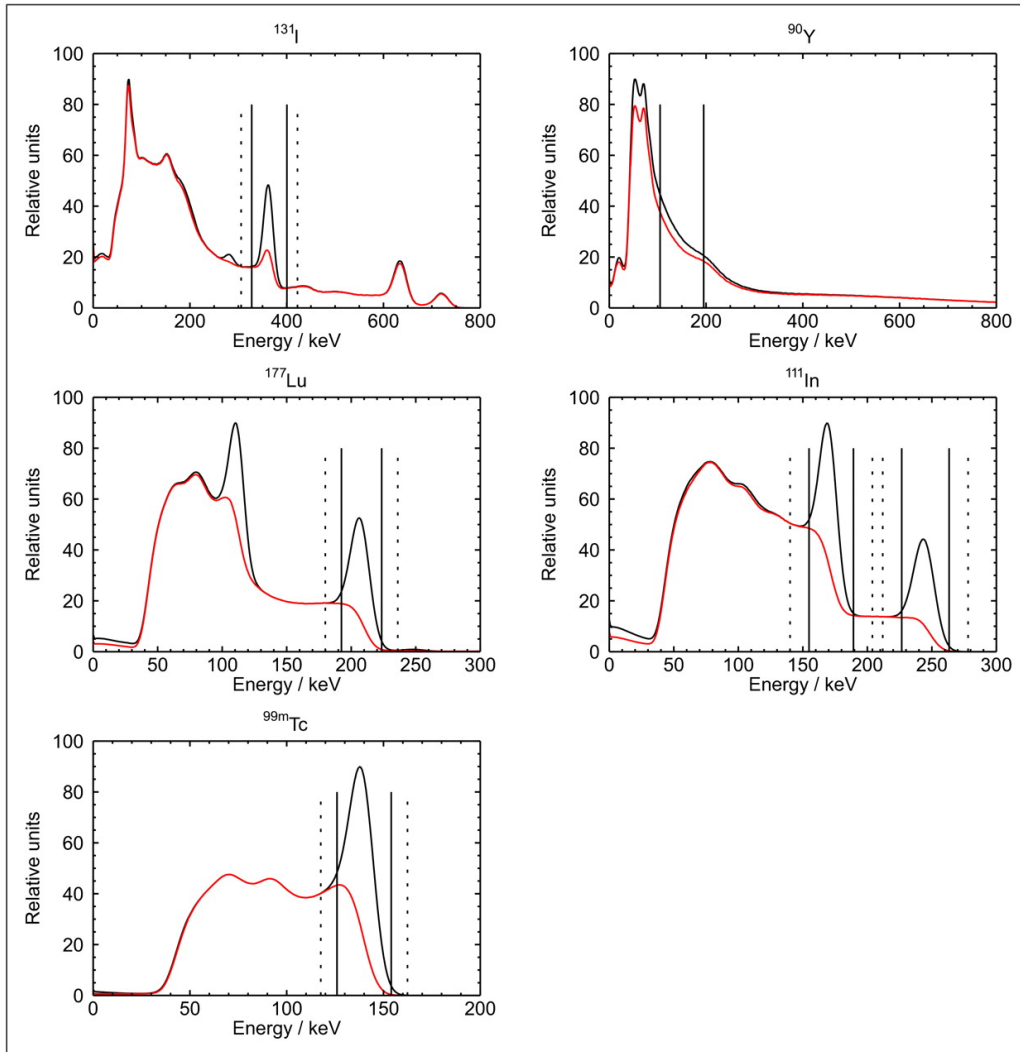


Figure 1.3: Energy spectra of some radionuclides used in internal radiotherapy, generated using SIMIND Monte Carlo simulation. This figure is published in [1], reprinted with permission of authors and the Society of Nuclear Medicine and Molecular Imaging, Inc.

the energy spectrum has clear photopeak of primary data as for I-131, the main acquisition window is often chosen around the peak and adjacent windows below and above the main window are used for scatter correction [1]. When there is no prominent photopeak of primary data as for Y-90, reasonable energy window is used with avoiding too high or too low energy range where the number of undesired scatter and penetration increases dramatically [3]. Sometimes, the fraction of primary count over total count is very small so that to get enough data for reconstruction, wider or multiple energy windows need to be used. Multiple acquisition windows can help improving quantitative accuracy and reducing noise.

1.1.3 Post-reconstruction Filtering

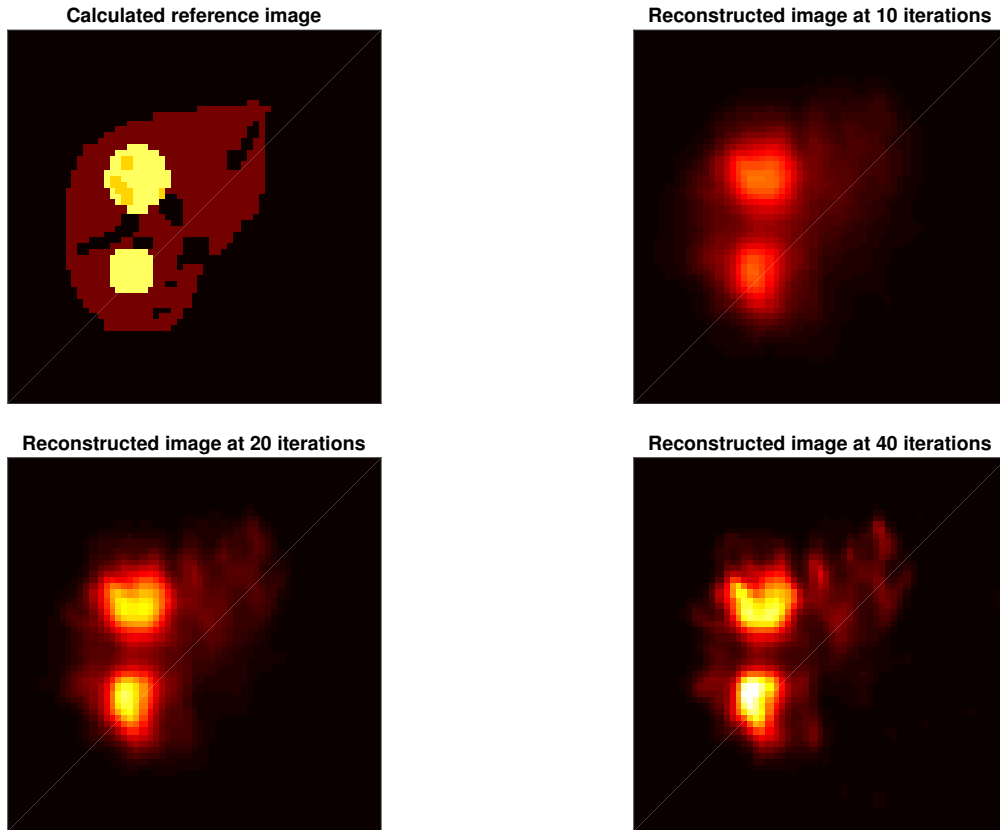


Figure 1.4: Reference and reconstructed image at different iteration number of a Y-90 SPECT.

SPECT image is typically corrupted by Poisson noise which is related to Poisson statistics of photons hitting detectors as well as noise propagating within the reconstruction process. Noise levels vary across the image and really depend on the reconstruction method. For example, filtered back-projection shows a global noise pattern which means different pixels have close noise levels while expectation-maximization algorithm shows the noise levels proportional to image intensities [4]. Besides, noise increases rapidly at high iteration of reconstruction which is sometimes necessary to recover accurate activity distributions. This is illustrated in Fig. 1.4. There is trade-off between obtaining more image detail and remaining an acceptable noise level. Sometimes it is desired to recover as much detail over a cancer region as possible without caring about more noise introduced over other regions. Sometimes an overall high quality image is needed. These kinds of decision reflect into choosing filtering parameters to optimize some metrics for image quality used to evaluate the filtering results such as recovery coefficient, peak signal-to-noise ratio, bias and variance.

Post-reconstruction filtering is used to suppress noise and edge artifacts at high iteration. A

good filter need to keep image details without blurring too much. Filter design can benefit from taking into account the mentioned noise properties. However, nonlinearity of reconstruction algorithm makes it hard to model noise exactly, and full understanding of noise properties in SPECT remains as a big research problem. General approach may approximate noise in reconstructed SPECT image with Gaussian distribution and assume either global or local noise variance.

Non-local means (NLM) filter has shown powerful denoising performance with well detail preserving for both natural images [5] and SPECT images [6]. Classical NLM filter uses the similarity between two local patches of a noisy image to determine weights in non-local adaptive smoothing [5]. NLM weights are obtained first by calculating the Euclidean distance between two local patches, denoted by d , and then by evaluating $\exp(-d^2/h^2)$ where h is a smoothing parameter. Therefore, higher weights can be assigned to pixels with similar patches so that edges and details may be well-preserved in non-local weighted averaging.

There are four different factors to determine output image quality of NLM in terms of weights. 1) The first factor is the similarity measure d . Other similarity measures have also been proposed such as hypothesis testing [7], principal component analysis (or subspace based method) [8, 9], blockwise aggregation [10], rotation-invariant measures [11–13], shape-adaptive patches [14], and patch based similarity with adaptive neighborhoods [15]. In multimodal medical imaging, inaccurate weights for noisy molecular images were enhanced by using additional high quality anatomical images [6, 16]. 2) The second factor is the strategy to determine a smoothing parameter h . Optimization strategies have been developed based on Stein’s unbiased risk estimation (SURE) for NLM with Gaussian noise [17, 18], NLM with Poisson noise [19], and blockwise NLM with Gaussian noise [20]. 3) The third factor is the function to use for weights such as $\exp(-x^2)$. Other functions have been proposed for weight calculation such as compact support functions [21, 22] and statistical distance functions [23, 24]. 4) The last factor is how to determine self-weight for the same pixel of input and output images.

The weights of NLM for two different pixels are essentially determined by the distance between two noisy local patches around these pixels and this distance is usually increased due to noise. However, weights for the same pixel or self-weights are not affected by noise in patches and the distance will be always 0 in the presence of noise. For an extremely noisy image, self-weights will be relatively too large compared to other weights, so that the filter output will be almost the same as the input noisy image. Therefore, using appropriate self-weight values can affect denoised image quality substantially. Investigating the strategies of determining optimal self-weights in NLM is an open problem for current researches.

1.2 Contribution of This Thesis

This work exploits methods to incorporate SPECT data of multiple energy windows in image reconstruction, with focus on Y-90 SPECT, commonly used in targeted radionuclide therapy. Previously, forward projection models with narrow single-energy window were used for image reconstruction from a single acquisition energy window. We propose a new Y-90 SPECT joint image reconstruction method from multiple acquisitions windows, referred to as joint spectral reconstruction (JSR) using multi-energy window forward models to improve the image quality further.

Furthermore, we propose novel self-weight estimation methods for NLM that account for bounded self-weights using Baranchik's minimax estimator [25], called local minimax self-weight estimation with direct bound (LMM-DB) and with reparametrization (LMM-RP). We first evaluate our proposed methods with a wide range of natural images as well as a real patient MRI image in various noise levels and confirm that our methods can be applied in a wide range of filtering applications. Then we apply the proposed methods to filter a SPECT image and yield good performance in terms of bias-variance trade-off, peak signal-to-noise (PSNR) ratio, and visual quality assessment. Our proposed methods also provide a heuristic way of choosing global smoothing parameters of NLM to yield PSNR values that are close to the optimal values without knowing the true image.

1.3 Organization of This Thesis

This thesis is organized as follows. Chapter II reviews some previous works on using multiple energy windows in Y-90 SPECT reconstruction, and proposes a joint spectral image reconstruction method. Chapter III reviews some previous works on strategies to estimate NLM self-weights, and proposes two local minimax self-weight estimation methods. Finally, chapter IV concludes this thesis with a summary and future works.

Joint Spectral Image Reconstruction for Y-90 SPECT

2.1 Related Works

Image reconstruction for Y-90 SPECT is challenging due to wide continuous energy spectrum of the bremsstrahlung photons (0-2.3 MeV). This wide spectrum was typically ignored in the past and a narrow energy window, such as 105-195 keV [26], was chosen for reconstruction. Because bremsstrahlung photon generation in tissue is an inefficient process (<2% of beta interactions in tissue-like material results in photons >50 keV [27]), it is desirable to include as many of the photons as possible.

Recently, there have been some research work dealing with continuous energy ranges in Y-90 image reconstruction [3, 28]. Rong *et al.* proposed to use a forward projection model to incorporate 4 energy windows with energy-dependent collimator detector response (CDR), attenuation, and scatter (ESSE) [3]. Elschot *et al.* proposed to use a fast Monte Carlo (MC) simulator as a forward projection in the reconstruction with 8 energy windows [28]. These methods improved the image quality of Y-90 SPECT significantly. Elschot *et al.* also compared their new Y-90 SPECT with Y-90 time-of-flight-PET and showed comparable results. In the previous two works, even though multi-energy was modeled inside the forward projector, only

a single-energy window acquisition window was selected based on trade-offs between several factors.

Exploiting the recent commercial availability of multi-window and list mode acquisition SPECT systems, in this work we propose a new Y-90 SPECT image reconstruction method that uses the multi-energy window measurements to improve the image quality further.

2.2 Methods

Two sets of 6 energy windows data were generated (narrow window: 105-135, 135-165, 165-195, 195-225, 225-255, 255-285 keV and wide window: 100-200, 200-300, 300-400, 400-500, 500-600, 600-700 keV) that are indexed $e = 1, \dots, 6$, for each set. The measurement for one energy window is modeled as

$$\mathbf{y}_e \sim \text{Poisson}(\mathbf{A}_e \mathbf{f}_e + \mathbf{s}_e). \quad (\text{II.1})$$

where e is an index for energy window, \mathbf{y}_e is a measurement for energy window e ; \mathbf{A}_e is a forward projector for energy window e with energy-dependent CDR and attenuation at the center of energy window e ; \mathbf{f}_e is an activity distribution in single-energy window e ; \mathbf{s}_e denotes a mean scatter for energy window e .

We denote the reconstruction of \mathbf{f}_1 from \mathbf{y}_1 the single spectral reconstruction (SSR), where the measurement and scatter are selected from the first energy window, and the projector is modeled with a single-energy window.

We propose a joint spectral reconstruction (JSR) method in which a single activity image is reconstructed from all energy window windows data with the following measurement model:

$$\begin{bmatrix} \mathbf{y}_1 \\ \vdots \\ \mathbf{y}_6 \end{bmatrix} \sim \text{Poisson} \left(\begin{bmatrix} \alpha_1 \mathbf{A}_1 \\ \vdots \\ \alpha_6 \mathbf{A}_6 \end{bmatrix} \mathbf{f} + \begin{bmatrix} \mathbf{s}_1 \\ \vdots \\ \mathbf{s}_6 \end{bmatrix} \right). \quad (\text{II.2})$$

where we model that $\mathbf{f}_e = \alpha_e \mathbf{f}$ with α_e obtained by measuring the ratio of the primary counts of window e to the primary counts of window 1. This joint model is similar to the model for motion-compensated image reconstruction using multiple motion frames in [29].

Energy and depth-dependent CDR was obtained from point source MC simulation with high energy collimator, then fitted using B-spline template for the last 3 wide windows and Gaussian model for the rest [30]. Energy-dependent attenuation was obtained by rescaling CT image for energy level of the center of each energy window e . Scatter was assumed to be known in these studies, but one can obtain the scatter contribution using MC scatter estimation methods [31].

MC simulation using SIMIND [32] coupled with XCAT phantom [33] was used to generate clinically realistic data corresponding to patient studies of Y-90 microsphere (glass) radioembolization in liver malignancies. Two lesions of size 80 mL (Tumor 1) and 41 mL (Tumor 2) were simulated in the liver with activity concentration ratio of liver:tumor:lung, 20:100:1. Before the addition of Poisson noise the projection data were scaled to the count level typical for a 30 min Y-90 SPECT scan performed at our clinic after a radioembolization procedure with around 3 GBq of Y-90.

The statistical image reconstruction of a Y-90 distribution can be obtained by performing the following constrained optimization problem:

$$\hat{\mathbf{f}} = \arg \max_{\mathbf{f} \geq 0} L(\mathbf{y}|\mathbf{f}) \quad (\text{II.3})$$

where L is a Poisson log-likelihood function, defined as equation II.4 and II.5 for SSR and JSR, respectively.

$$L(\mathbf{y}|\mathbf{f}) = \sum_i y_i \log \bar{y}_i(\mathbf{f}) - \bar{y}_i(\mathbf{f}) \quad (\text{II.4})$$

$$L(\mathbf{y}|\mathbf{f}) = \sum_e \sum_i [y_e]_i \log [\bar{y}_e(\mathbf{f})]_i - [\bar{y}_e(\mathbf{f})]_i \quad (\text{II.5})$$

where \bar{y}_i is the mean of y_i - the i th element of the measurement \mathbf{y} . This optimization problem was solved using the ordered-subsets expectation-maximization (OSEM) algorithm [34] with up to 100 iterations, 6 subsets.

Reconstructed images were evaluated based on recovery coefficient (RC), standard deviation (SD), and bias within a region of interest (ROI) on a tumor or healthy liver (liver part not containing any tumor) calculated as in (II.6-II.8). For tumor, ROI is its whole area, and for healthy liver, ROI is a sphere area on the liver, away from tumors to avoid spill-out effect.

$$\text{RC} = \frac{\text{measured count in ROI}}{\text{true count in ROI}} \quad (\text{II.6})$$

$$\text{SD} = \frac{1}{\bar{\mathbf{f}}_{\text{ROI}}} \sqrt{\frac{1}{N-1} \sum_{i \in \text{ROI}} (\hat{\mathbf{f}}[i] - \bar{\mathbf{f}}_{\text{ROI}})^2} \quad (\text{II.7})$$

$$\text{Bias} = \frac{1}{N} \sum_{i \in \text{ROI}} |\hat{\mathbf{f}}_{\text{noiseless}}[i] - \mathbf{f}_{\text{true}}[i]| \quad (\text{II.8})$$

The true image, \mathbf{f}_{true} , was created using the masks and known activity concentration ratio of liver, tumor, and lung, and scaled to have the same activity level as \mathbf{f}_1 . N is the number of

pixels in ROI . \bar{f}_{ROI} is the average of \hat{f} calculated in ROI . $\hat{f}_{noiseless}$ is the image reconstructed from noiseless data. $f[i]$ is the i th element of f .

2.3 Results

Fig. 2.1 shows the normalized CDR profiles for the measurement and corresponding fitting method. For low energy windows (narrow windows: $e = 1, \dots, 6$, and wide windows: $e = 1, \dots, 3$), Gaussian fitting is sufficient to match the measured CDR values. However, for high energy windows (wide windows: $e = 4, \dots, 6$), B-spline template fitting is needed to yield the accurate fit for the obvious penetration tails on the CDR.

2.3.1 Results for Narrow Windows

Fig. 2.2 compares RC, SD, and Bias obtained by JSR and SSR. Significantly higher RC values and lower SD using JSR were observed compared to using SSR for both ROIs. These improvement tend to be much larger as the iteration number increases. At the 100th iteration, JSR yielded up to 11.19% increase in RC and up to 46.9% decrease in SD compared to SSR. That proves the advantage of using multiple acquisition windows in improving RC and SD. In terms of bias, however, JSR was not as good as SSR, which can be explained that using smaller amount of data in SSR can generally achieves the lower bias. Fig. 2.3 LEFT shows that the visual image quality of the reconstructed image using JSR is better than that using SSR.

Table 2.1: Percentage at which each measure at the 100th iteration increases while changing from SSR to JSR (NARROW windows).

	RC	SD	Bias
Tumor1 (80 mL)	2.91	-32.6	14.14
Tumor2 (41 mL)	11.19	-46.9	11.19
Liver	2.06	-38.27	29.99

2.3.2 Results for Wide Windows

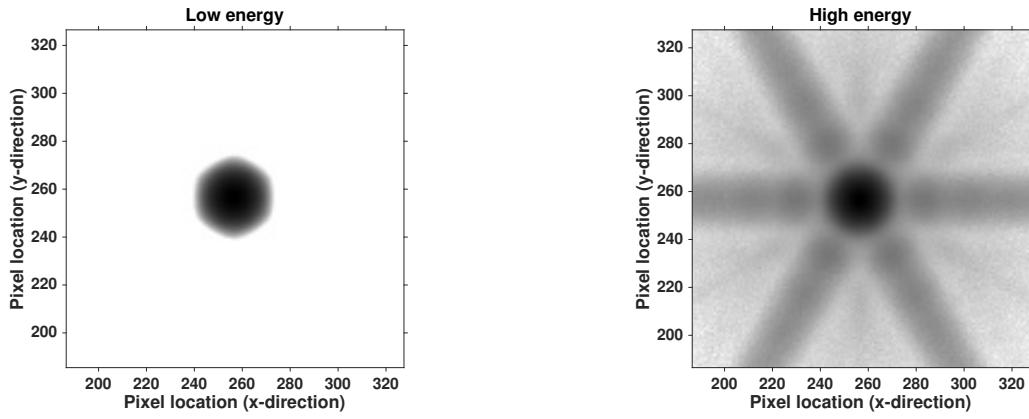
For wide window case (Fig. 2.2), the same trends as in narrow window case were obtained for both RC, SD, and Bias. The improvement was relatively higher in RC, but lower in SD. At the 100th iteration, JSR yielded up to 19.23% increase in RC and up to 19.01% decrease in SD compared to SSR.

Table 2.2: Percentage at which each measure at the 100th iteration increases while changing from SSR to JSR (WIDE windows).

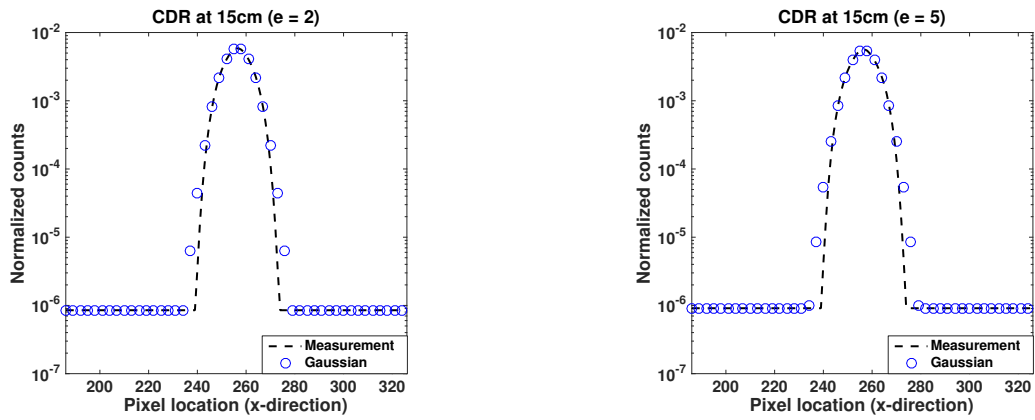
	RC	SD	Bias
Tumor1 (80 mL)	18.19	-14.36	25.74
Tumor2 (41 mL)	19.23	-9.53	21.28
Liver	14.52	-19.01	74.19

2.4 Discussion

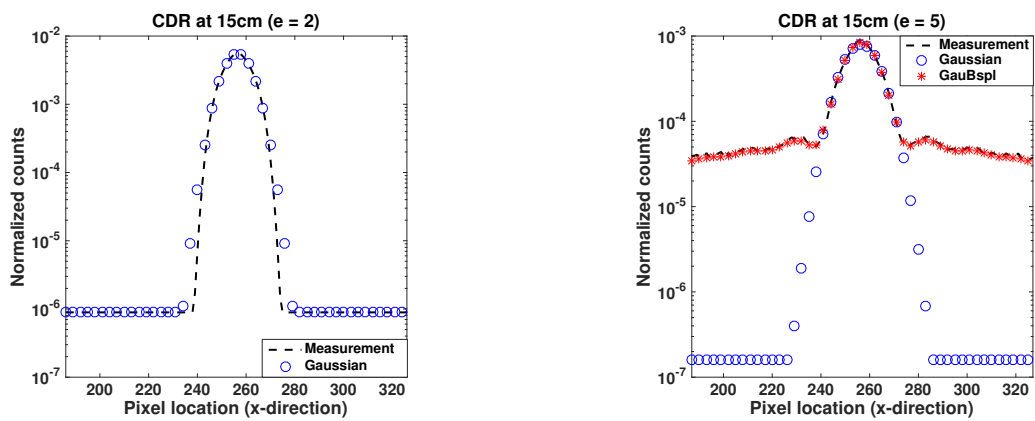
JSR with multiple energy window models and acquisition windows considerably improved the Y-90 SPECT image reconstruction quality over SSR. The improvement in noise demonstrated here is particularly significant because bremsstrahlung photon production in tissue is inefficient and SPECT count levels can be low, especially in systemic therapies with Y-90.



(a) Example of MC simulated CDR



(b) Fitting CDR (Narrow window)



(c) Fitting CDR (Wide window)

Figure 2.1: MC simulated and fitted CDR using Gaussian/B-spline (all in log scale).

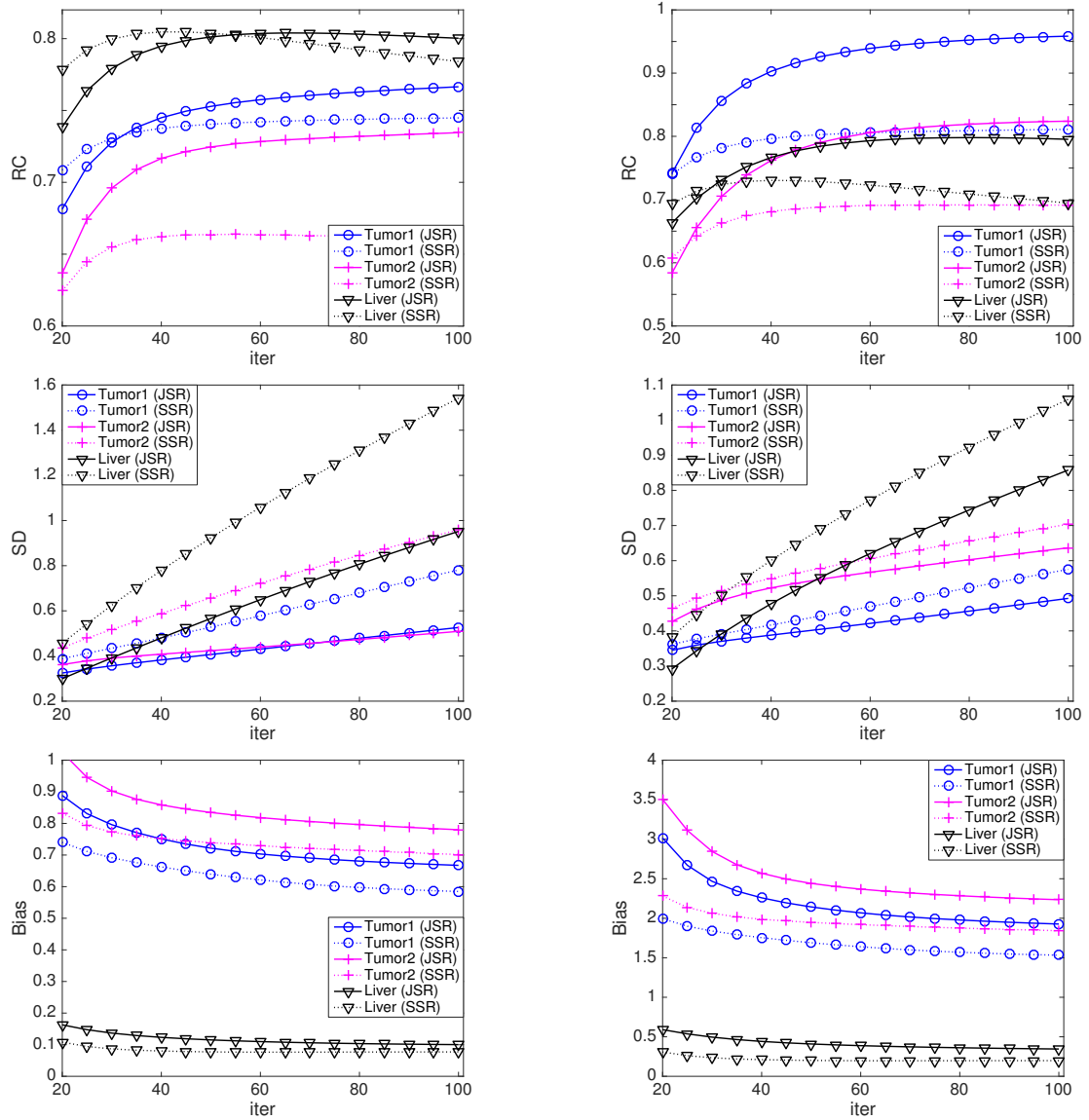


Figure 2.2: RC, SD, and Bias for narrow window case (LEFT) and wide window case (RIGHT).

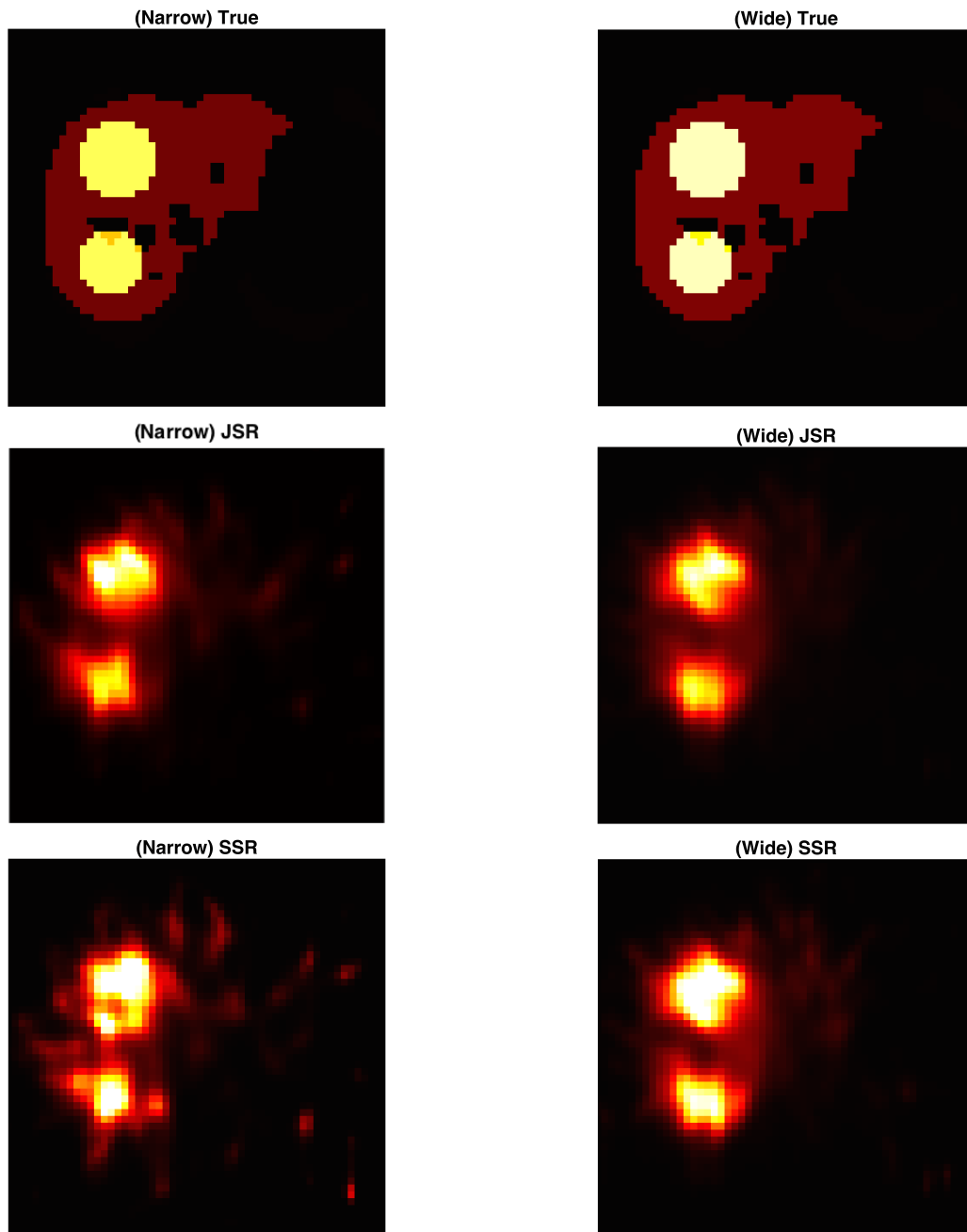


Figure 2.3: True and reconstructed images at 35 iteration for narrow and wide window cases.

Post-reconstruction Non-local Means Filtering

3.1 Related Works

For the classical NLM filter by Buades *et al.*, self-weights were set to be 1 or the maximum weight in a neighborhood [5]. These strategies guarantee at least one or two largest weights are the same, respectively. Doré *et al.* also used the maximum weight in a neighborhood as self-weight, but only if that maximum weight is large [35]. Brox *et al.* proposed a method to have at least n number of the same largest weights [36], and Zimmer *et al.* considered self-weight as a free parameter to estimate [37]. Salmon *et al.* developed a SURE-based method for self-weights to account for noise [38].

Recently, Wu *et al.* proposed a method to determine self-weights using James-Stein (JS) type estimator [2]. The idea of this work is to use JS estimator to determine a reparametrized self-weight in a local neighborhood (called local JS estimator or LJS). The LJS method yielded the best peak signal-to-noise ratio (PSNR) results over other existing methods [5, 38]. However, it has a couple of limitations. First of all, the LJS can yield self-weights much larger than 1 theoretically since no upper bound for self-weights was assumed. This may lead to severe rare patch artifacts. Secondly, the original LJS method has been tested with a relatively large local neighborhood for determining a self-weight assuming that self-weights are the same in the local neighborhood. However, too large local neighborhood size may introduce strong bias in the resulting denoised images.

In this paper, we investigate the original LJS method in terms of the local neighborhood size for self-weight estimation, and excessive self-weight estimation when no upper bound is applied on the self-weight. We then propose novel self-weight estimation methods for NLM that account for bounded self-weights using Baranchik’s minimax estimator [25], called local minimax self-weight estimation with direct bound (LMM-DB) and with reparametrization (LMM-RP). Our proposed methods were evaluated with a wide range of natural images, a real patient MRI image, and a SPECT image in various noise levels in terms of PSNR as well as other performance criteria such as bias-variance trade-off curve and visual quality assessment. Our proposed methods were compared with classical NLM filter using self-weight 1 [5] and the original LJS method [2], which is already shown to be the best among all other previous self-weight determination methods.

3.2 Review on Local James-Stein Self-Weight Estimation for Non Local Means Filter

We will briefly review the classical NLM filter proposed by Buades *et al.* [5] and the original LJS method proposed by Wu *et al.* [2].

3.2.1 Reviewing Classical Non-Local Means Filter

Let’s assume that an image \mathbf{x} is contaminated by noise \mathbf{n} with the following model:

$$\mathbf{y} = \mathbf{x} + \mathbf{n} \quad (\text{III.1})$$

where \mathbf{n} is zero-mean white Gaussian noise with standard deviation σ . A NLM filtered value at the pixel i is a weighted average of all pixels in a search region Ω_i :

$$\hat{x}_i = \frac{\sum_{j \in \Omega_i} w_{i,j} y_j}{\sum_{j \in \Omega_i} w_{i,j}} \quad (\text{III.2})$$

where y_i is the i th element of \mathbf{y} , $w_{i,j}$ is a weight between the i th and j th pixels, and Ω_i is the set of all pixels in a small area around the i th pixel or the entire image. The similarity weight of the classical NLM is defined as:

$$w_{i,j} = \exp\left(\frac{-\|\mathbf{P}_i \mathbf{y} - \mathbf{P}_j \mathbf{y}\|^2}{2|\mathbf{P}|h^2}\right) \quad (\text{III.3})$$

where \mathbf{P}_i is an operator to extract a square-shaped patch centered at the i th pixel, $\|\cdot\|$ is an l_2 norm, $|\mathbf{P}|$ is the number of pixels within a patch, and h is a global smoothing parameter. Equation (III.3) implies that self-weights $w_{i,i}$ are always equal to 1. Previous works on self-weights have shown that good strategies for determining self-weights affect the image quality of NLM filtering [2, 5, 35, 38].

3.2.2 Reviewing Local James-Stein Self-Weight Estimation

The LJS method was proposed to determine $w_{i,i}$ as follows [2]. Firstly, (III.2) was decomposed into two terms:

$$\hat{x}_i = \frac{W_i}{W_i + w_{i,i}} \hat{z}_i + \frac{w_{i,i}}{W_i + w_{i,i}} y_i \quad (\text{III.4})$$

where

$$W_i = \sum_{j \in \Omega_i \setminus \{i\}} w_{i,j}$$

and

$$\hat{z}_i = \sum_{j \in \Omega_i \setminus \{i\}} w_{i,j} y_j / W_i. \quad (\text{III.5})$$

The terms \hat{z}_i do not contain $w_{i,i}$. Then, the LJS method reparametrized (III.4) using

$$p_i = \frac{w_{i,i}}{W_i + w_{i,i}} \quad (\text{III.6})$$

so that (III.4) becomes

$$\hat{x}_i = (1 - p_i) \hat{z}_i + p_i y_i. \quad (\text{III.7})$$

The problem of estimating self-weights $w_{i,i}$ became the problem of estimating p_i . Lastly, the JS estimator [39, 40] for p_i was proposed:

$$p_i^{\text{LJS}} = 1 - \frac{(|\mathbf{B}| - 2) \sigma^2}{\|\mathbf{B}_i \mathbf{y} - \mathbf{B}_i \hat{\mathbf{z}}\|^2} \quad (\text{III.8})$$

where \mathbf{B}_i is an operator to extract a square-shaped neighborhood centered at the i th pixel, $|\mathbf{B}|$ is the number of pixels within that neighborhood, and σ is known noise level.

Equation (III.8) implies that $p_i^{\text{LJS}} \in (-\infty, 1]$. Since weights are non-negative, it was proposed to use the zero-lower bound for p_i^{LJS} as follows [2]:

$$\hat{x}_i^{\text{LJS}+} = \left(1 - p_i^{\text{LJS}+}\right) \hat{z}_i + p_i^{\text{LJS}+} y_i \quad (\text{III.9})$$

where

$$p_i^{\text{LJS}_+} := [p_i^{\text{LJS}}]_+ = \left[1 - \frac{(|\mathbf{B}| - 2) \sigma^2}{\|\mathbf{B}_i \mathbf{y} - \mathbf{B}_i \hat{\mathbf{z}}\|^2} \right]_+ \quad (\text{III.10})$$

and $[s]_+ := \max(s, 0)$. Wu *et al.* also mentioned that a user-defined upper bound for p_i can be used, but did not investigate upper bound further [2].

3.3 Limitations of Local James-Stein Self-Weight Estimation for Non Local Means Filter

We will investigate two limitations of the original LJS method [2] in terms of the size of local neighborhoods for self-weight estimation and possible excessive self-weight estimation.

3.3.1 Size of Local Neighborhood for Self-Weight Estimation

Even though it was not mentioned in [2], there were two implicit steps to obtain the LJS self-weight estimator (III.10). The first step is to choose a local set of pixels around the i th pixel, called this set Ω_i^B , corresponding to the operator \mathbf{B}_i and assume that

$$\hat{x}_j = (1 - p_i) \hat{z}_j + p_i y_j, \quad j \in \Omega_i^B. \quad (\text{III.11})$$

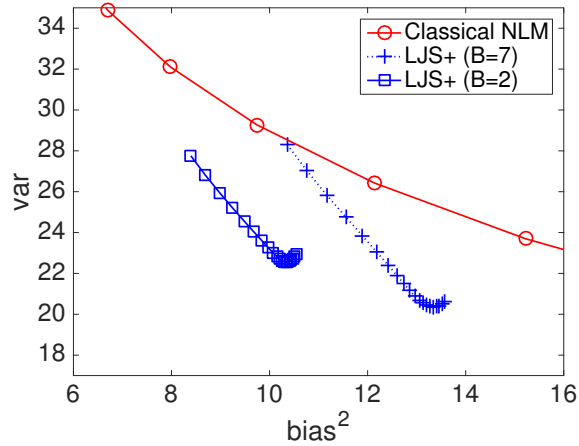


Figure 3.1: Bias-variance curves (cameraman example) for the classical NLM and the LJS method (LJS₊) for different sizes of local neighborhood (B). The curves are plotted with varying the smoothing parameter h ($\log_2 h \in [1.8, 3.2]$).

Based on the works of Stein [39] and James and Stein [40], if $|\mathbf{B}| \geq 3$, then for a small neighborhood Ω_i^B extracted by \mathbf{B}_i ,

$$\hat{x}_j = \left(1 - p_i^{\text{LJS}+}\right) \hat{z}_j + p_i^{\text{LJS}+} y_j, \quad j \in \Omega_i^B. \quad (\text{III.12})$$

is a dominating estimator for x_j “locally” in Ω_i^B . The LJS method used the zero lower bound for estimating p_i to obtain a realistic self-weight value that is not negative. It was also a good choice in terms of estimator performance since this positive part of JS estimator is dominating over the original JS estimator according to the works of Baranchik [25,41] and Efron and Morris [42].

The second implicit step is to assign the resulting p_i^{LJS} to p_i in (III.7) only for the single pixel i so that

$$\hat{x}_i^{\text{LJS}} = \left(1 - p_i^{\text{LJS}}\right) \hat{z}_i + p_i^{\text{LJS}} y_i. \quad (\text{III.13})$$

Wu *et al.* evaluated the LJS method with $|\mathbf{B}| = 15 \times 15$ [2], which looks relatively large.

According to this two implicit step interpretation, we can conjecture that using smaller size of $|\mathbf{B}|$ may be more desirable for less biased estimate of p_i since the assumption of having the same p_i in Ω_i^B is less likely to be true for larger size of Ω_i^B . Fig. 3.1 confirms our conjecture. The bias-variance curves of the LJS method yielded better bias-variance trade-offs than the classical NLM method for both large local neighborhood with the half window size $B = 7$ ($|\mathbf{B}| = 15 \times 15$) and small local neighborhood with $B = 2$ ($|\mathbf{B}| = 5 \times 5$). However, using larger local neighborhood size for estimating p_i yielded stronger bias than using smaller size for the same level of variance.

3.3.2 Excessively Large Self-Weight Estimation

In the original LJS method for determining self-weights by estimating p_i 's [2], it is theoretically possible that self-weights have excessively high values. For example, (III.6) suggests that if $p_i = 1$ and $W_i > 0$, then $w_{i,i} \gg 1$. Slight artifacts in the background area potentially due to possible excessive self weight estimates were observed in [2] where relatively larger neighborhood size $|\mathbf{B}| = 15 \times 15$ was used. We observed much more severe visual image quality degradation on the background area if the size of $|\mathbf{B}|$ in (III.8) is small as shown in the top left figure of Fig. 3.2.

We investigated this issue with an example of cameraman image. This example was denoised using the original LJS method [2], but with a smaller neighborhood size $|\mathbf{B}| = 5 \times 5$. For areas with more details such as edges and textures, large p_i values were estimated to yield high self-weights as shown in the top right figure of Fig. 3.2. However, since W_i 's are also very small on

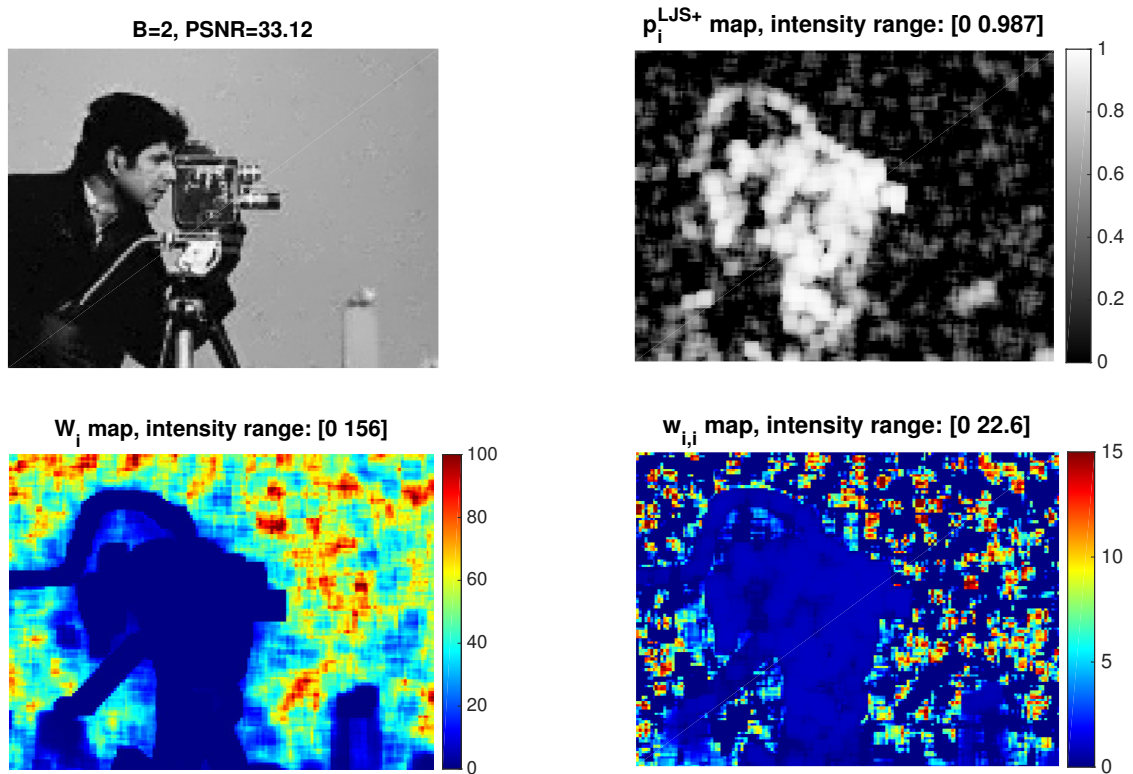


Figure 3.2: Denoised image of cameraman example using the original LJS method [2] with no upper bound for self-weights (top left), estimated p_i values (top right), calculated W_i 's (bottom left), and resulting self-weights ($w_{i,i}$) showing excessive self-weights (bottom right). $B = 2$ and $\sigma = 10$.

these areas as shown in the bottom left figure of Fig. 3.2, the resulting self-weight map yielded values close to 1 on areas with details.

In contrast, for areas with almost no details such as flat intensity background, relatively smaller p_i values were estimated. Some of them were much larger than 0 and the rest of them were closer to 0 as shown in the top right figure of Fig. 3.2. However, since W_i values for flat areas were relatively large as shown in the bottom left figure of Fig. 3.2, some estimated p_i values of the original LJS method (LJS+) were estimated to yield excessively large self-weights that were much larger than 1 as shown in the bottom right figure of Fig. 3.2. Therefore, these excessively large self-weights caused severe rare patch artifacts for filtered image so that visual quality degradation was observed as shown in the top left figure of Fig. 3.2.

3.4 Local Minimax Estimation Methods for Upper Bounded Self-Weights in Non Local Means Filter

In this section, we propose two local self-weight estimation methods that account for upper bounded self-weights using Baranchik's minimax estimator [25].

3.4.1 Bounded Self-Weights

It is usually assumed that self-weight $w_{i,i} \in [0, 1]$. However, there are many possible upper bounds for self-weight such as 1 [5] or some positive value that is possibly less than 1 based on SURE [38]. In this paper, two different upper bound values $w_{i,i}^{\max}$ for self-weights were evaluated such that $0 \leq w_{i,i} \leq w_{i,i}^{\max}$. One maximum self-weight value is

$$w_{i,i}^{\max\text{-one}} = 1 \quad (\text{III.14})$$

which was a usual choice for self-weight in the classical NLM method [5]. The other maximum value is

$$w_{i,i}^{\max\text{-stein}} = \exp(-\sigma^2/h^2) \quad (\text{III.15})$$

which was motivated by the SURE based NLM self-weights [38]. We assume that σ is known and h is pre-determined so that this upper bound for self-weights can also be determined in advance. Equation (III.15) takes noise level into account. As σ is smaller, the maximum self-weight (III.15) is closer to one or (III.14). However, the difference between (III.15) and (III.14) will be larger at higher noise level.

Since p_i is estimated instead of $w_{i,i}$, it is necessary to derive the range of p_i corresponding to $0 \leq w_{i,i} \leq w_{i,i}^{\max}$. From (III.6), the derivative of p_i with respect to $w_{i,i}$ is non-negative as follows:

$$\frac{d}{dw_{i,i}} p_i = \frac{W_i}{(W_i + w_{i,i})^2} \geq 0$$

since $W_i \geq 0$. Therefore, p_i is an increasing function of $w_{i,i}$ and for $0 \leq w_{i,i} \leq w_{i,i}^{\max}$, the range of p_i will be

$$0 \leq p_i \leq \frac{w_{i,i}^{\max}}{W_i + w_{i,i}^{\max}} =: p_i^{\max} \leq 1.$$

Note that if $W_i = 0$, then $p_i^{\max} = 1$. The estimator $p_i^{\text{LJS}^+}$ in (III.10) automatically guarantees that $0 \leq p_i \leq 1$ if $|\mathbf{B}| \geq 2$. However, since $W_i > 0$ holds practically for almost any real images with noise, it is necessary to constrain p_i to be less than or equal to the upper bound p_i^{\max} , which is usually less than one.

3.4.2 Local Minimax Self-Weight Estimation with Direct Bound

Enforcing the upper limit p_i^{\max} on the estimated p_i (III.10) using $\min(p_i^{\text{LJS}^+}, p_i^{\max})$ breaks the optimality of the JS estimator if $p_i^{\max} < 1$. In this paper, we propose to use Baranchik's minimax estimator [25] instead to incorporate bounded self-weights into the estimator (see Baranchik [25], Efron and Morris [42], and Strawderman [43] for more details on this minimax estimator).

Theorem 1 (Baranchik) For $\mathbf{y} \sim \mathcal{N}_r(\mathbf{x}, \sigma^2 \mathbf{I})$, $r \geq 3$, and loss $L(\mathbf{x}, \hat{\mathbf{x}}) = \|\mathbf{x} - \hat{\mathbf{x}}\|$, an estimator of the form $\hat{\mathbf{x}} = q\mathbf{y}$ where

$$q = \left[1 - c(\|\mathbf{y}\|) \frac{\sigma^2(r-2)}{\|\mathbf{y}\|^2} \right] \quad (\text{III.16})$$

is minimax provided

(i) $0 \leq c(\|\mathbf{y}\|) \leq 2$ and

(ii) the function c is nondecreasing.

Here \mathbf{y} shrinks toward 0 which is the initial estimation of \mathbf{x} .

The original JS estimator and its positive part are special cases of the Baranchik's minimax estimator. For the original JS estimator (III.8),

$$c(\|\mathbf{s}\|) = 1 \quad (\text{III.17})$$

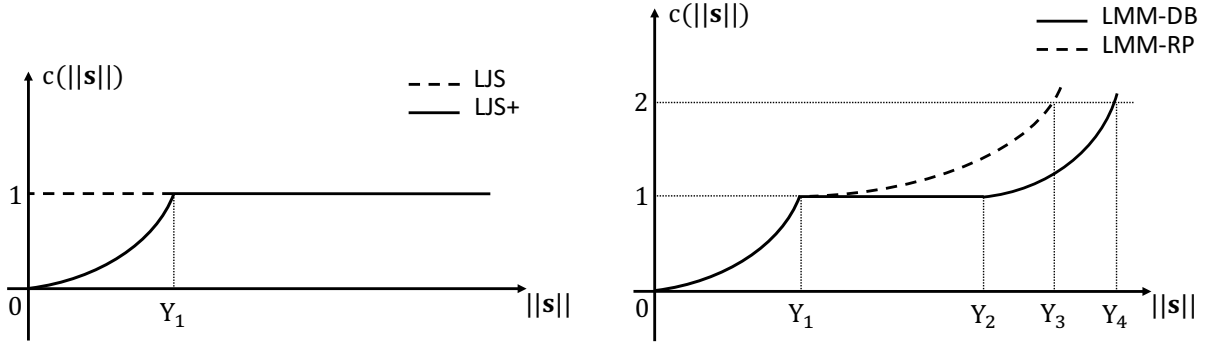
where $\mathbf{s} = \mathbf{B}_i \mathbf{y} - \mathbf{B}_i \hat{\mathbf{z}}$ so that it satisfies both conditions (i, ii) of the Baranchik's theorem. In the positive-part estimator (III.9), it can be shown that

$$c(\|\mathbf{s}\|) = \begin{cases} \frac{\|\mathbf{s}\|^2}{\sigma^2(r-2)}, & 0 \leq \|\mathbf{s}\| \leq Y_1 \\ 1, & \text{otherwise} \end{cases} \quad (\text{III.18})$$

where $Y_1 := \sigma\sqrt{r-2}$. The original and positive part JS estimators are illustrated in Fig. 3.3 (a).

We propose a new local minimax self-weight estimation method using direct bound with a specific upper-bound value as follows:

$$p_i^{\text{LMM-DB}} := \min(p_i^{\text{LJS}^+}, p_i^{\max}).$$



(a) Original and positive-part JS estimators (b) Proposed minimax estimators with bounds

Figure 3.3: Graphical illustrations of the original and positive part JS estimators without upper bounds and the proposed minimax self-weight estimators with upper bounds in terms of $c(\|\mathbf{s}\|)$ vs. $\|\mathbf{s}\|$.

The theory behind this operation is the Baranchik’s minimax estimator theorem. According to it, this operation can be interpreted as follows:

$$c(\|\mathbf{s}\|) = \begin{cases} \frac{\|\mathbf{s}\|^2}{\sigma^2(r-2)}, & 0 \leq \|\mathbf{s}\| \leq Y_1 \\ 1, & Y_1 < \|\mathbf{s}\| \leq Y_2 \\ \frac{\|\mathbf{s}\|^2(1-p^{\max})}{\sigma^2(r-2)}, & Y_2 < \|\mathbf{s}\| \end{cases} \quad (\text{III.19})$$

where

$$Y_2 := \sigma \sqrt{\frac{r-2}{1-p^{\max}}}.$$

We call this local minimax self-weight estimator using direct bound (LMM-DB) and this estimator is illustrated in Fig. 3.3 (b) where

$$Y_4 := \sigma \sqrt{\frac{2(r-2)}{1-p^{\max}}}$$

Note that LMM-DB is not minimax anymore for $\|\mathbf{s}\| > Y_4$. Fortunately, $\|\mathbf{s}\| = \|\mathbf{B}_i \mathbf{y} - \mathbf{B}_i \hat{\mathbf{z}}\|$ can be limited by adjusting a smoothing parameter h (setting it smaller) so that all $\|\mathbf{s}\| \leq Y_4$ and $c(\|\mathbf{B}_i \mathbf{y} - \mathbf{B}_i \hat{\mathbf{z}}\|) \leq 2$. Then, LMM-DB becomes “practically” a minimax estimator. Let us denote by h^{\max} the maximum h that satisfies $\|\mathbf{s}\| \leq Y_4$.

In this case, one question can be raised: Will the optimal h fall into this range of h that satisfies $\|\mathbf{s}\| \leq Y_4$? Interestingly, our simulations with many natural images showed that the

optimal smoothing parameter h^* based on the true images is very close to h^{\max} . This is because LMM-DB yielded $p^{\max} \rightarrow 1$ (so that $Y_2 \rightarrow \infty$) or almost all $\|\mathbf{B}_i \mathbf{y} - \mathbf{B}_i \hat{\mathbf{z}}\|$ were less than or equal to Y_4 . Therefore, $p_i^{\text{LMM-DB}}$ is “practically” minimax based on the Baranchik’s theorem for many natural images. Moreover, LMM-DB may provide a way of choosing the optimal smoothing parameter value h without knowing the underlying true image. We will investigate this issue empirically in Section V.

3.4.3 Local Minimax Self-Weight Estimation with Reparametrization

LMM-DB set p to be the same p^{\max} for a wide range of $\|\mathbf{B}_i \mathbf{y} - \mathbf{B}_i \hat{\mathbf{z}}\|$ values. We propose another new method called local minimax self-weight estimation with reparametrization (LMM-RP) that assigns different p values for different $\|\mathbf{B}_i \mathbf{y} - \mathbf{B}_i \hat{\mathbf{z}}\|$.

We reparametrized p_i in (III.7) in the following way:

$$\begin{aligned}\hat{x}_i &= \hat{z}_i + (p_i/p_i^{\max})p_i^{\max}(y_i - \hat{z}_i) \\ &= \hat{z}_i + p_i^{\text{T}}(y_i^{\text{T}} - \hat{z}_i^{\text{T}})\end{aligned}\tag{III.20}$$

$$= (1 - p_i^{\max})\hat{z}_i + \hat{z}_i^{\text{T}} + p_i^{\text{T}}(y_i^{\text{T}} - \hat{z}_i^{\text{T}})\tag{III.21}$$

where $\hat{z}_i^{\text{T}} = p_i^{\max}\hat{z}_i$, $y_i^{\text{T}} = p_i^{\max}y_i$, and

$$p_i^{\text{T}} = \frac{1}{p_i^{\max}} \frac{w_{i,i}}{W_i + w_{i,i}}.\tag{III.22}$$

Note that for $0 \leq w_{i,i} \leq w_{i,i}^{\max}$, p_i^{T} is an increasing function of $w_{i,i}$ and the range of p_i^{T} will be $0 \leq p_i^{\text{T}} \leq 1$. We propose to use the positive part JS estimator to estimate reparametrized p_i^{T} as follows:

$$\begin{aligned}p_i^{\text{T,LJS}_+} &= \left[1 - \frac{(|\mathbf{B}| - 2)(p_i^{\max})^2 \sigma^2}{\|\mathbf{B}_i \mathbf{y}^{\text{T}} - \mathbf{B}_i \hat{\mathbf{z}}^{\text{T}}\|^2} \right]_+ \\ &= \left[1 - \frac{(|\mathbf{B}| - 2) \sigma^2}{\|\mathbf{B}_i \mathbf{y} - \mathbf{B}_i \hat{\mathbf{z}}\|^2} \right]_+ = p_i^{\text{LJS}_+}.\end{aligned}\tag{III.23}$$

This method is equivalent to using a multiplicative factor p_i^{\max} for the original JS shrinkage (III.9) as follows:

$$\hat{x}_i^{\text{LMM-RP}} = (1 - p_i^{\text{LMM-RP}})\hat{z}_i + p_i^{\text{LMM-RP}}y_i\tag{III.24}$$

where

$$p_i^{\text{LMM-RP}} = p_i^{\max} \left[1 - \frac{(|\mathbf{B}| - 2) \sigma^2}{\|\mathbf{B}_i \mathbf{y} - \mathbf{B}_i \hat{\mathbf{z}}\|^2} \right]_+.\tag{III.25}$$

This proposed estimator, LMM-RP, is not dominating for estimating x_i , but rather dominating for estimating $p_i^{\max}x_i$ as shown in (III.21). Thus, the positive part JS estimator does not guarantee that LMM-RP is dominating.

Table 3.1: PSNR (dB) summary (mean \pm standard deviation) for various natural images.

		B = 2					B = 7					
	σ	Classical NLM	LJS,	LMM-DB ^{one}	LMM-RP ^{one}	LMM-DB ^{stein}	LMM-RP ^{stein}	LJS,	LMM-DB ^{one}	LMM-RP ^{one}	LMM-DB ^{stein}	LMM-RP ^{stein}
<i>cameraman</i>	10	32.42 \pm 0.034	33.12 \pm 0.031	33.32 \pm 0.030	33.29 \pm 0.029	33.17 \pm 0.029	33.04 \pm 0.030	32.98 \pm 0.035	33.10 \pm 0.036	33.05 \pm 0.037	32.98 \pm 0.038	32.85 \pm 0.040
	20	28.48 \pm 0.052	29.12 \pm 0.052	29.46 \pm 0.056	29.29 \pm 0.056	29.27 \pm 0.060	28.97 \pm 0.052	29.32 \pm 0.062	29.34 \pm 0.059	29.04 \pm 0.054	29.11 \pm 0.058	28.80 \pm 0.049
	40	25.35 \pm 0.059	25.39 \pm 0.083	25.89 \pm 0.075	26.11 \pm 0.082	26.08 \pm 0.087	25.74 \pm 0.079	25.98 \pm 0.073	25.98 \pm 0.073	25.94 \pm 0.080	25.96 \pm 0.083	25.63 \pm 0.076
	60	23.19 \pm 0.065	22.88 \pm 0.062	23.39 \pm 0.055	23.74 \pm 0.065	23.67 \pm 0.069	23.54 \pm 0.061	23.68 \pm 0.068	23.69 \pm 0.068	23.62 \pm 0.071	23.63 \pm 0.070	23.54 \pm 0.059
<i>lena</i>	10	33.90 \pm 0.018	34.52 \pm 0.017	34.74 \pm 0.017	34.81 \pm 0.018	34.77 \pm 0.017	34.69 \pm 0.017	34.82 \pm 0.020	34.83 \pm 0.020	34.80 \pm 0.019	34.76 \pm 0.018	34.63 \pm 0.018
	20	30.78 \pm 0.031	30.90 \pm 0.023	31.25 \pm 0.033	31.50 \pm 0.032	31.51 \pm 0.032	31.31 \pm 0.029	31.51 \pm 0.031	31.51 \pm 0.031	31.45 \pm 0.028	31.48 \pm 0.031	31.27 \pm 0.029
	40	27.64 \pm 0.032	26.94 \pm 0.028	27.74 \pm 0.033	28.08 \pm 0.029	28.08 \pm 0.029	28.06 \pm 0.028	28.10 \pm 0.028	28.10 \pm 0.028	28.07 \pm 0.028	28.08 \pm 0.029	28.06 \pm 0.028
	60	25.60 \pm 0.052	24.38 \pm 0.040	25.66 \pm 0.051	26.02 \pm 0.052	26.01 \pm 0.053	26.02 \pm 0.054	26.01 \pm 0.051	26.02 \pm 0.054	26.02 \pm 0.054	26.02 \pm 0.053	26.02 \pm 0.054
<i>montage</i>	10	34.68 \pm 0.045	35.19 \pm 0.043	35.60 \pm 0.042	35.67 \pm 0.039	35.65 \pm 0.042	35.55 \pm 0.045	35.12 \pm 0.049	35.39 \pm 0.046	35.38 \pm 0.042	35.46 \pm 0.045	35.34 \pm 0.047
	20	30.35 \pm 0.088	30.74 \pm 0.062	31.29 \pm 0.067	31.38 \pm 0.070	31.40 \pm 0.078	31.06 \pm 0.068	31.00 \pm 0.076	31.13 \pm 0.073	31.07 \pm 0.068	31.18 \pm 0.068	30.81 \pm 0.063
	40	26.24 \pm 0.063	26.30 \pm 0.072	26.98 \pm 0.070	27.29 \pm 0.063	27.30 \pm 0.064	27.20 \pm 0.061	27.01 \pm 0.052	27.03 \pm 0.052	27.04 \pm 0.055	27.08 \pm 0.053	27.00 \pm 0.053
	60	23.76 \pm 0.104	23.48 \pm 0.116	24.16 \pm 0.113	24.61 \pm 0.115	24.60 \pm 0.106	24.38 \pm 0.115	24.33 \pm 0.092	24.33 \pm 0.092	24.36 \pm 0.090	24.37 \pm 0.088	24.16 \pm 0.095
<i>house</i>	10	34.57 \pm 0.038	35.02 \pm 0.039	35.36 \pm 0.041	35.38 \pm 0.039	35.34 \pm 0.043	35.29 \pm 0.046	35.31 \pm 0.042	35.32 \pm 0.043	35.25 \pm 0.044	35.21 \pm 0.047	35.12 \pm 0.045
	20	31.43 \pm 0.063	31.54 \pm 0.048	32.13 \pm 0.050	32.39 \pm 0.048	32.39 \pm 0.050	32.19 \pm 0.067	32.30 \pm 0.052	32.31 \pm 0.054	32.26 \pm 0.058	32.30 \pm 0.056	32.10 \pm 0.068
	40	27.62 \pm 0.044	27.18 \pm 0.038	27.84 \pm 0.049	28.37 \pm 0.037	28.37 \pm 0.039	28.33 \pm 0.045	28.35 \pm 0.041	28.35 \pm 0.041	28.34 \pm 0.045	28.35 \pm 0.042	28.33 \pm 0.045
	60	25.01 \pm 0.092	24.24 \pm 0.087	25.17 \pm 0.098	25.65 \pm 0.095	25.65 \pm 0.087	25.65 \pm 0.088	25.65 \pm 0.088	25.65 \pm 0.088	25.65 \pm 0.088	25.66 \pm 0.087	25.65 \pm 0.088
<i>pepper</i>	10	32.62 \pm 0.056	33.37 \pm 0.042	33.53 \pm 0.048	33.56 \pm 0.049	33.49 \pm 0.051	33.39 \pm 0.050	33.28 \pm 0.043	33.37 \pm 0.040	33.35 \pm 0.042	33.33 \pm 0.042	33.17 \pm 0.042
	20	28.94 \pm 0.031	29.54 \pm 0.029	29.78 \pm 0.040	29.88 \pm 0.038	29.86 \pm 0.028	29.51 \pm 0.027	29.77 \pm 0.027	29.79 \pm 0.027	29.70 \pm 0.026	29.73 \pm 0.024	29.34 \pm 0.033
	40	25.31 \pm 0.050	25.50 \pm 0.057	25.67 \pm 0.041	26.12 \pm 0.049	26.11 \pm 0.054	25.97 \pm 0.055	26.08 \pm 0.054	26.08 \pm 0.054	26.04 \pm 0.056	26.05 \pm 0.054	25.95 \pm 0.055
	60	22.99 \pm 0.048	22.95 \pm 0.091	23.18 \pm 0.061	23.80 \pm 0.067	23.80 \pm 0.071	23.78 \pm 0.075	23.81 \pm 0.070	23.81 \pm 0.070	23.79 \pm 0.074	23.80 \pm 0.073	23.78 \pm 0.075
<i>barbara</i>	10	32.93 \pm 0.026	33.50 \pm 0.018	33.66 \pm 0.020	33.70 \pm 0.021	33.66 \pm 0.022	33.53 \pm 0.020	33.72 \pm 0.017	33.74 \pm 0.017	33.69 \pm 0.017	33.66 \pm 0.017	33.44 \pm 0.017
	20	29.36 \pm 0.032	29.83 \pm 0.029	29.96 \pm 0.032	30.23 \pm 0.030	30.27 \pm 0.028	30.04 \pm 0.029	30.27 \pm 0.029	30.27 \pm 0.028	30.19 \pm 0.026	30.24 \pm 0.027	30.00 \pm 0.030
	40	25.68 \pm 0.047	25.78 \pm 0.048	25.79 \pm 0.047	26.46 \pm 0.043	26.51 \pm 0.040	26.51 \pm 0.039	26.52 \pm 0.040	26.52 \pm 0.040	26.51 \pm 0.039	26.51 \pm 0.040	26.51 \pm 0.039
	60	23.50 \pm 0.032	23.17 \pm 0.039	23.57 \pm 0.034	24.13 \pm 0.037	24.15 \pm 0.035	24.16 \pm 0.035	24.15 \pm 0.036	24.15 \pm 0.036	24.16 \pm 0.035	24.16 \pm 0.035	24.16 \pm 0.035
<i>boat</i>	10	31.78 \pm 0.015	32.73 \pm 0.019	32.81 \pm 0.018	32.82 \pm 0.017	32.72 \pm 0.015	32.61 \pm 0.016	32.73 \pm 0.018	32.75 \pm 0.018	32.72 \pm 0.017	32.65 \pm 0.017	32.49 \pm 0.017
	20	28.40 \pm 0.017	29.14 \pm 0.017	29.23 \pm 0.019	29.37 \pm 0.015	29.34 \pm 0.015	29.05 \pm 0.015	29.30 \pm 0.018	29.30 \pm 0.018	29.25 \pm 0.017	29.27 \pm 0.017	28.95 \pm 0.018
	40	21.95 \pm 0.053	25.45 \pm 0.021	25.45 \pm 0.021	26.01 \pm 0.016	25.99 \pm 0.016	25.92 \pm 0.014	25.98 \pm 0.012	25.98 \pm 0.012	25.95 \pm 0.013	25.96 \pm 0.012	25.92 \pm 0.014
	60	23.64 \pm 0.025	23.11 \pm 0.028	23.72 \pm 0.026	24.01 \pm 0.026	24.01 \pm 0.025	23.99 \pm 0.025	24.01 \pm 0.025	24.01 \pm 0.025	24.00 \pm 0.025	24.00 \pm 0.025	23.99 \pm 0.025
<i>hill</i>	10	31.87 \pm 0.029	32.63 \pm 0.020	32.67 \pm 0.019	32.71 \pm 0.018	32.61 \pm 0.018	32.47 \pm 0.014	32.67 \pm 0.016	32.67 \pm 0.016	32.64 \pm 0.016	32.55 \pm 0.015	32.34 \pm 0.013
	20	28.82 \pm 0.022	29.23 \pm 0.031	29.23 \pm 0.031	29.48 \pm 0.024	29.48 \pm 0.023	29.29 \pm 0.023	29.45 \pm 0.021	29.45 \pm 0.021	29.41 \pm 0.023	29.42 \pm 0.022	29.25 \pm 0.024
	40	25.91 \pm 0.022	25.70 \pm 0.026	25.98 \pm 0.024	26.36 \pm 0.024	26.38 \pm 0.022	26.37 \pm 0.022	26.38 \pm 0.022	26.38 \pm 0.022	26.37 \pm 0.022	26.38 \pm 0.022	26.37 \pm 0.022
	60	24.25 \pm 0.017	23.45 \pm 0.013	24.32 \pm 0.018	24.60 \pm 0.024	24.59 \pm 0.024	24.60 \pm 0.024	24.59 \pm 0.022	24.59 \pm 0.022	24.60 \pm 0.024	24.60 \pm 0.024	24.60 \pm 0.024
<i>couple</i>	10	31.80 \pm 0.014	32.76 \pm 0.009	32.81 \pm 0.009	32.85 \pm 0.010	32.80 \pm 0.011	32.71 \pm 0.011	32.76 \pm 0.013	32.77 \pm 0.013	32.75 \pm 0.012	32.72 \pm 0.011	32.59 \pm 0.012
	20	28.14 \pm 0.023	28.93 \pm 0.023	28.93 \pm 0.023	29.16 \pm 0.028	29.16 \pm 0.029	28.86 \pm 0.030	29.11 \pm 0.028	29.11 \pm 0.028	29.07 \pm 0.029	29.08 \pm 0.029	28.76 \pm 0.030
	40	24.93 \pm 0.035	25.03 \pm 0.026	25.05 \pm 0.026	25.49 \pm 0.026	25.50 \pm 0.030	25.44 \pm 0.032	25.48 \pm 0.031	25.48 \pm 0.031	25.47 \pm 0.030	25.47 \pm 0.030	25.43 \pm 0.032
	60	23.25 \pm 0.037	22.76 \pm 0.043	23.29 \pm 0.036	23.59 \pm 0.045	23.60 \pm 0.044	23.59 \pm 0.044	23.60 \pm 0.044	23.60 \pm 0.044	23.59 \pm 0.044	23.60 \pm 0.044	23.59 \pm 0.044
<i>fingerprint</i>	10	30.27 \pm 0.017	30.87 \pm 0.015	30.87 \pm 0.016	30.84 \pm 0.016	30.80 \pm 0.017	30.57 \pm 0.016	30.88 \pm 0.018	30.88 \pm 0.019	30.83 \pm 0.019	30.81 \pm 0.020	30.50 \pm 0.018
	20	26.64 \pm 0.010	27.06 \pm 0.014	27.06 \pm 0.014	27.04 \pm 0.014	27.12 \pm 0.012	26.72 \pm 0.013	27.10 \pm 0.012	27.10 \pm 0.012	26.93 \pm 0.013	27.05 \pm 0.013	26.70 \pm 0.012
	40	23.20 \pm 0.018	23.68 \pm 0.024	23.68 \pm 0.024	23.96 \pm 0.023	24.06 \pm 0.022	24.05 \pm 0.023	24.05 \pm 0.022	24.05 \pm 0.022	24.05 \pm 0.022	24.05 \pm 0.022	24.05 \pm 0.023
	60	20.93 \pm 0.034	21.44 \pm 0.029	21.44 \pm 0.029	21.85 \pm 0.041	21.97 \pm 0.037	21.98 \pm 0.037	21.98 \pm 0.037	21.98 \pm 0.037	21.98 \pm 0.037	21.98 \pm 0.037	21.98 \pm 0.037
<i>MRI</i>	10	40.06 \pm 0.043	39.19 \pm 0.040	40.81 \pm 0.033	40.89 \pm 0.032	40.83 \pm 0.034	40.71 \pm 0.029	40.79 \pm 0.040	40.85 \pm 0.038	40.83 \pm 0.037	40.81 \pm 0.038	40.61

are very close to each other in the case of LMM-RP, too, for many natural images. Therefore, LMM-RP is “practically” minimax.

3.5 Simulation Results

3.5.1 Simulation Setup

Ten natural images¹ (cameraman, lena, montage, house, pepper, barbara, boat, hill, couple, fingerprint) were used in our study as noise-free images (256×256 or 512×512 pixels, 8 bits). A real patient MRI (512×512 pixels, 8 bits), acquired and processed under institutional review board (IRB) approved protocols, was also used. Each input image was added with white Gaussian noise of various standard deviations $\sigma \in \{10, 20, 40, 60\}$. Then, we evaluated the proposed method with a SPECT generated from XCAT phantom, in which known true image with intensity range [0-126] is added with i.i.d. Gaussian noise of $\sigma = 3$.

All algorithms were implemented using MATLAB R2015b (The Mathworks, Inc., Natick, MA, USA). Patch size and search window size of NLM filter were chosen to be 7×7 and 31×31 , respectively, which were the same as [2]. Both conventional LJS and proposed algorithms were tested for $B = 1, \dots, 9$ where $|\mathbf{B}| = (2B + 1)^2 > 3$.

A global smoothing parameter h was chosen empirically to yield the best PSNR:

$$\text{PSNR}(\hat{\mathbf{x}}) = 10 \log_{10} \frac{255^2}{\|\hat{\mathbf{x}} - \mathbf{x}\|^2 / N} \quad (\text{III.27})$$

where N is the size of image. In addition to PSNR, mean bias vs. mean variance trade-off curves were used as performance measure for different smoothing parameter values h where

$$\overline{\text{bias}^2} = \frac{1}{N} \sum_{i=1}^N (\bar{x}_i - x_i)^2 \quad (\text{III.28})$$

$$\overline{\text{var}} = \frac{1}{N} \sum_{i=1}^N \frac{1}{k-1} \sum_{j=1}^k (\hat{x}_{ij} - \bar{x}_i)^2 \quad (\text{III.29})$$

where N is the size of image, k is the number of realizations (20 in our simulation), \hat{x}_{ij} is the j th estimation at i th pixel, and \bar{x}_i is the mean of \hat{x}_{ij} or

$$\bar{x}_i = \frac{1}{k} \sum_{j=1}^k \hat{x}_{ij}.$$

¹Available online at: http://www.cs.tut.fi/~foi/GCF-BM3D/BM3D_images.zip as the date of 16 Nov. 2015.

Visual quality assessment was also performed.

3.5.2 Performance Studies with PSNR

For a fixed neighborhood size B to estimate p_i 's, the optimal NLM smoothing parameter h^* was determined to maximize PSNR. In our proposed methods, two maximum self-weights in (III.14) and (III.15) were used. LMM-DB and LMM-RP with (III.14) are denoted by LMM-DB^{one} and LMM-RP^{one}. LMM-DB and LMM-RP with (III.15) are denoted by LMM-DB^{stein} and LMM-RP^{stein}. Table 3.1 summarizes quantitative PSNR results for 12 images with different noise levels. For large $B = 7$ our proposed LMM-DB and LMM-RP methods based on Baranchik's minimax estimator yielded much better PSNR results than the classical NLM method [5] and comparable PSNR to the original LJS method based on James-Stein estimator [2]. For small $B = 2$, our proposed LMM-DB and LMM-RP methods yielded better PSNR than LJS.

3.5.3 Performance Studies with Bias-Variance Trade-Off

Bias-variance trade-off was investigated with many natural images. As shown in Fig. 3.1, a neighborhood size B for estimating p_i using LJS method [2] was a significant factor to determine bias. This tendency was also observed for other different natural images as illustrated in Fig. 3.4. Increasing B for LJS method moves bias-variance trade-off curves to the bottom right direction so that bias was increased and variance was decreased. However, the role of the smoothing parameter h changed for LJS method. Unlike classical NLM method (see the bias-variance curve of NLM in Fig. 3.1), increasing a smoothing parameter h beyond a certain point for LJS method did not decrease variance anymore for all natural images that we tested. This is because increasing h will also increase p_i values so that the resulting LJS estimator becomes closer to the noisy input image y_i due to no bound for self-weights.

Our proposed methods (LMM-DB, LMM-RP) yielded trade-off curves that have decreased variance for increased smoothing parameter h , and yielded bias-variance curves that are lower than or equal to LJS method for fixed B and σ . This tendency was observed with various natural images and SPECT image as illustrated in Fig. 3.4. It was important to choose an appropriate neighborhood size B for LJS method to obtain a certain level of bias, but our proposed methods can achieve that bias level by adjusting the smoothing parameter h , which is the same as classical NLM. It seems that using LMM-RP has slightly more advantages than using LMM-DB in terms of PSNR as shown in Table 3.1 and bias-variance trade-off curves as shown in Fig. 3.4 for high noise level.

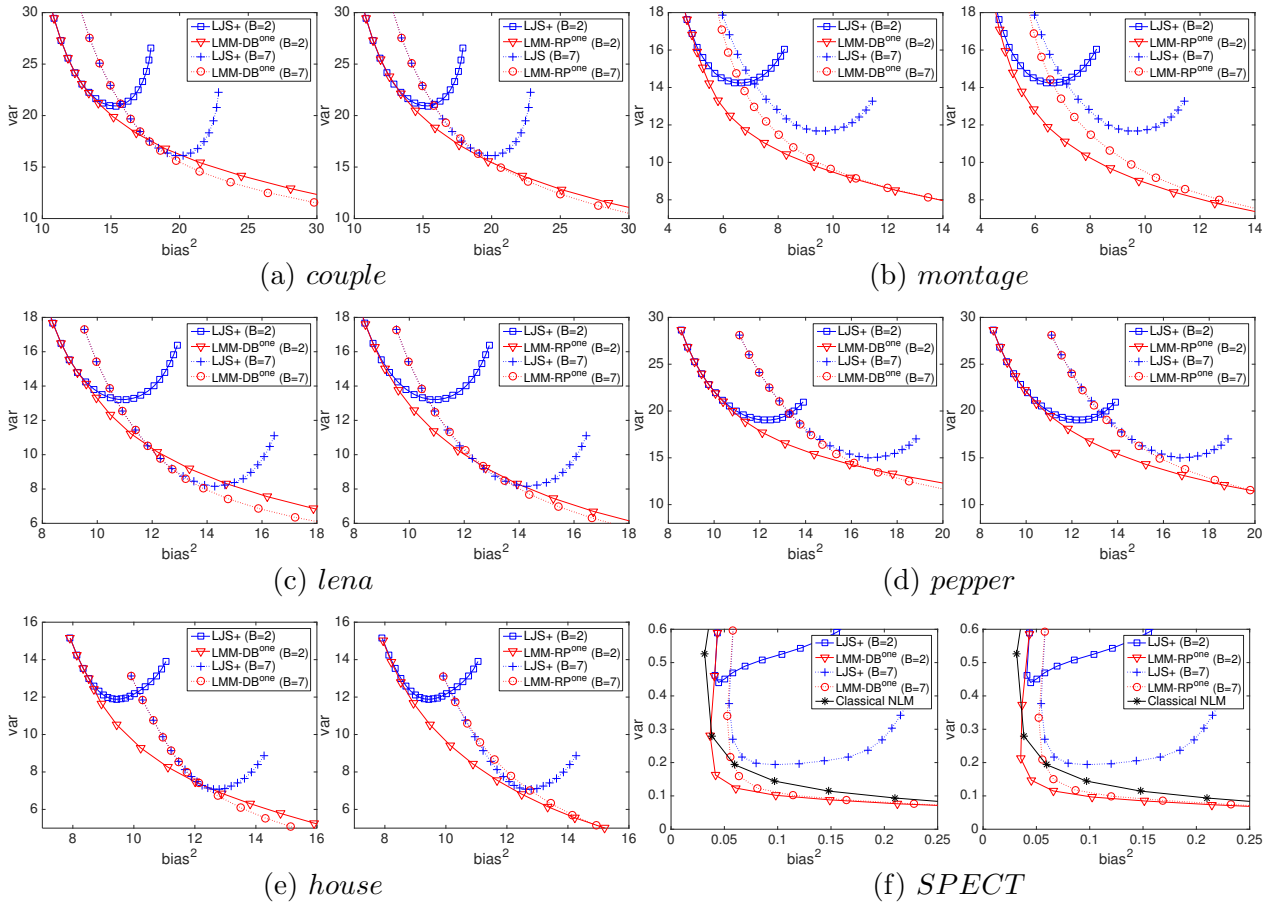


Figure 3.4: Bias-variance curves for natural images using LJS₊ [2] and our proposed LMM – DB^{one}, LMM – RP^{one} methods with a noise level $\sigma = 10$.

3.5.4 Performance Studies with Visual Quality Assessment

The most important improvements of our proposed LMM-DB and LMM-RP methods over LJS method were achieved in terms of visual quality. Fig. 3.5 (a) shows the true cameraman image (left) and noisy image (right) with noise level of $\sigma = 10$. Fig. 3.5 (b) presents filtered images using LJS method [2]) with $B = 2$ and $B = 7$. Severe artifacts were observed on the background areas when using $B = 2$ and these artifacts were reduced when using $B = 7$. However, there are still some artifacts near the edges of objects. Our proposed LMM-DB and LMM-RP yielded more reduced artifacts than LJS method for both $B = 2, 7$. This tendency was also observed in SPECT image and many natural images as shown in Fig. 3.6, 3.7, especially on high intensity flat areas. PSNR improvement of LJS method was achieved with severe (when $B = 2$) or mild (when $B = 7$) artifacts, but our proposed methods achieved both high PSNR and much more reduced visual artifacts. Reduced visual artifacts can be important in some applications such as diagnostic medical imaging.

3.5.5 Maximum Self-Weights: One vs. Stein’s

Two maximum self-weights were proposed to use: one in (III.14) that was proposed in [5] and Stein’s in (III.15) that was proposed in [38]. Fig. 3.8 shows that LMM – DB^{one} yielded better bias-variance curve and PSNR than LMM – DB^{stein} when the noise level was low. For high noise level $\sigma = 40$, LMM – DB^{stein} yielded better PSNR and bias-variance curve than LMM – DB^{one}. However, these differences were not significant and image-dependent, which are also illustrated in terms of PSNR in Table 3.1. In terms of visual quality, no significant difference was observed for both methods.

3.5.6 “Practical” Minimax Estimator

Table 3.2: Percentage (%) of $c(\|\mathbf{s}\|)$ that exceed 2 using LMM – DB and LMM – RP methods, $\sigma = 10$, $B = 2$.

		$\sigma = 10$	$\sigma = 20$	$\sigma = 40$	$\sigma = 60$
<i>cameraman</i>	LMM-DB ^{one}	0.32	0.04	0.03	0.05
	LMM-DB ^{stein}	0.85	0.66	0.21	0.18
<i>fingerprint</i>	LMM-DB ^{one}	0.00	0.00	0.00	0.00
	LMM-DB ^{stein}	0.30	0.13	0.09	0.02
<i>MRI</i>	LMM-DB ^{one}	0.10	0.05	0.10	0.13
	LMM-DB ^{stein}	0.18	0.16	0.16	0.16

		$\sigma = 10$	$\sigma = 20$	$\sigma = 40$	$\sigma = 60$
<i>cameraman</i>	LMM-RP ^{one}	0.25	0.04	0.01	0.00
	LMM-RP ^{stein}	1.07	0.90	0.20	0.22
<i>fingerprint</i>	LMM-RP ^{one}	0.01	0.00	0.00	0.00
	LMM-RP ^{stein}	0.27	0.19	0.13	0.03
<i>MRI</i>	LMM-RP ^{one}	0.09	0.05	0.07	0.09
	LMM-RP ^{stein}	0.23	0.20	0.16	0.13

The proposed LMM-DB and LMM-RP methods are minimax as far as $\|\mathbf{s}\| \leq Y_4$ and $\|\mathbf{s}\| \leq Y_3$, respectively, as shown in Fig. 3.3. However, these conditions impose upper bounds for smoothing parameters h so that the optimal h^* that yields the best PSNR may not be achievable. We empirically investigate this issue with many natural images.

Table 3.2 shows the ratio (percentage unit) of the number of pixels that $c(\|\mathbf{s}\|) > 2$ to the total number of pixels for cameraman, fingerprint, and MRI images when the optimal h^* for the highest PSNR was chosen based on the true images for proposed LMM-DB and LMM-RP methods. For most of the pixels, LMM-DB and LMM-RP were minimax. The relationship between the percentage of pixels with $c(\|\mathbf{s}\|) > 2$ and the root mean squared error (RMSE) is illustrated in Fig. 3.9 for cameraman and SPECT images. Surprisingly, the optimal smoothing parameters h for the lowest RMSE point (or the highest PSNR) of LMM-DB and LMM-RP

methods are very close to the smoothing parameters h such that the percentage of $c(\|\mathbf{s}\|) > 2$ is 0.1%. This phenomenon was not just for these two images. As shown in Table 3.3, the pixel percentage of $c(\|\mathbf{s}\|) > 2$ that does not require to know the true image can determine smoothing parameters that yielded comparable PSNR values to the best PSNR's yielded by using optimal smoothing parameters calculated based on knowledge of the true image. This was observed for all other images used in our simulations, with different noise levels, and when $B = 2$ is used. However, the criteria of using the pixel percentage of $c(\|\mathbf{s}\|) > 2$ did not work for $B = 7$ well in our simulations. This criteria can be potentially used for choosing a smoothing parameter without knowing the true image with our proposed methods as a heuristic approach. More analytical investigation on this criteria can be an interesting extension of this work.

3.6 Discussion

The classical NLM method was a significant work in image denoising [5] and it requires to determine two important parameters for good denoising performance: a smoothing parameter and a self-weight value. The LJS method proposed by Wu *et al.* [2] developed a state-of-the-art method for self-weight determination using JS estimation [40] and yielded superior results in terms of PSNR compared to other existing methods. However, since the LJS method did not impose the upper bound for self-weight estimation, the bias can not be controlled by a smoothing parameter anymore and visual quality degradation was experienced. Our proposed methods based on the Baranchik's minimax theorem [25] yielded comparable PSNR results to the state-of-the-art LJS method. By imposing the upper bounds for self-weights, bias-variance trade-off can be controlled by a smoothing parameter again and substantial visual artifact reduction was achieved.

The minimax property of our proposed methods depends on the choice of smoothing parameters. When using sufficiently small smoothing parameters, LMM-DB and LMM-RP are minimax "practically" according to the Baranchik's theorem [25]. However, when using large smoothing parameters, there may be some pixels that are not minimax for self-weight estimation. More empirical investigation showed that the optimal smoothing parameter h to yield the best PSNR only results in very small portion of pixels that do not have minimax self-weight estimators. In fact, this can be used as a heuristic way to choose a good smoothing parameter since testing minimax properties of our proposed methods does not require the true image when $B = 2$. Therefore, our proposed methods do not only provide an optimal way to determine self-weights, but also provide a heuristic way to determine a good smoothing parameter.

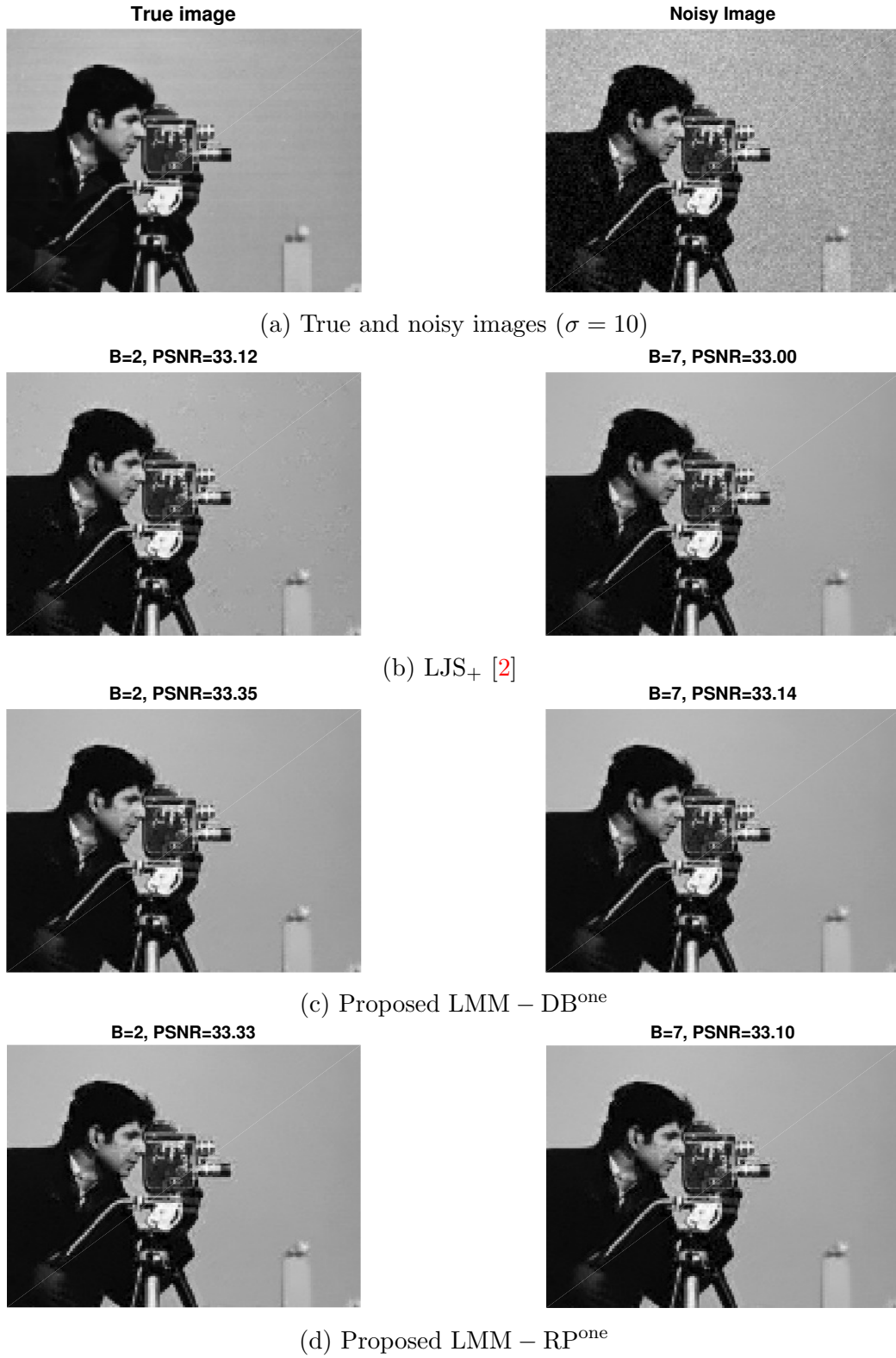
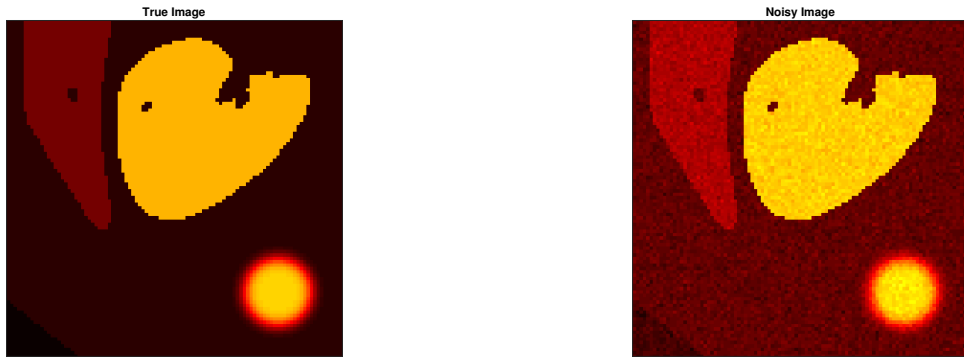


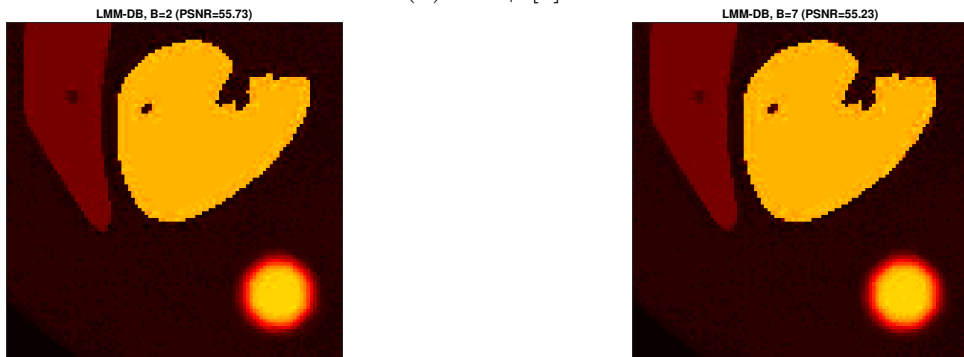
Figure 3.5: Cameraman: True, noisy ($\sigma = 10$), and filtered images using LJS₊ [2], proposed LMM – DB^{one}, and LMM – RP^{one}.



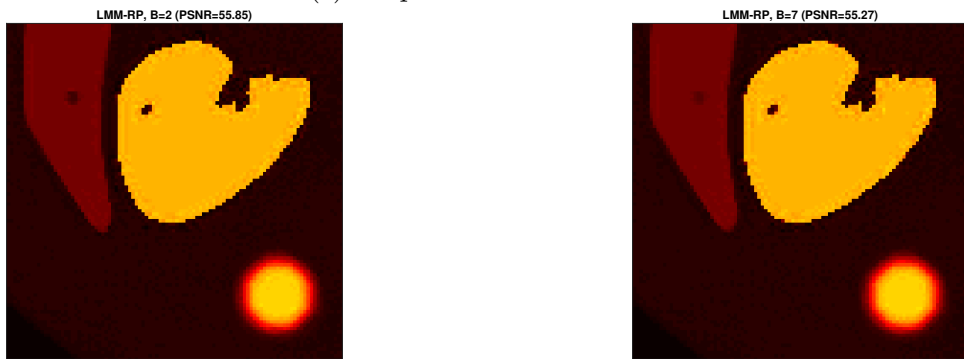
(a) True and noisy images ($\sigma = 3$)



(b) LJS₊ [2]



(c) Proposed LMM – DB^{one}



(d) Proposed LMM – RP^{one}

Figure 3.6: SPECT: True, noisy ($\sigma = 3$), and filtered images using LJS₊ [2], proposed LMM – DB^{one}, and LMM – RP^{one}.

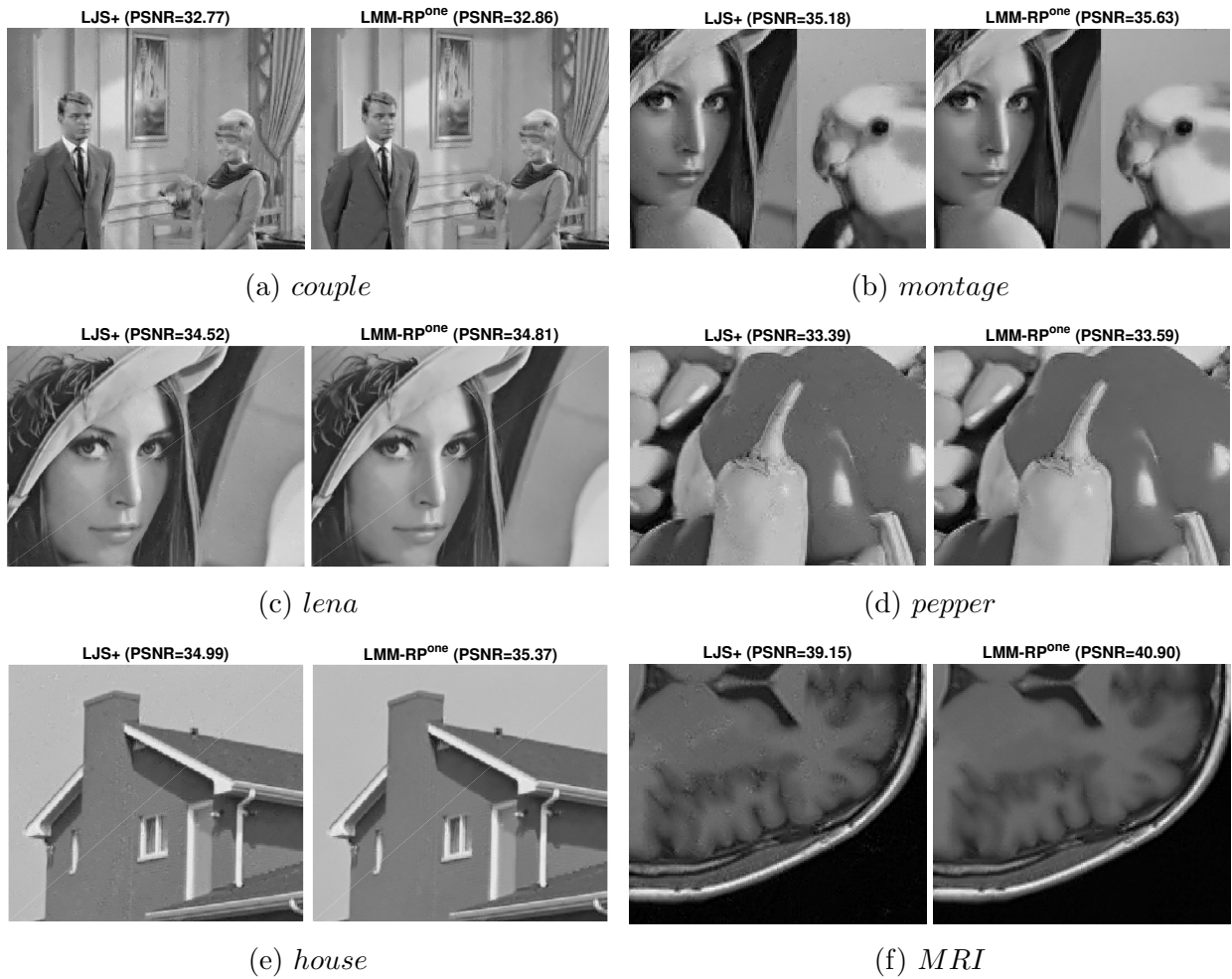


Figure 3.7: Filtered results for various natural images using LJS₊ [2] and proposed LJS – RP^{one} with noise level $\sigma = 10$ and neighborhood size $B = 2$.

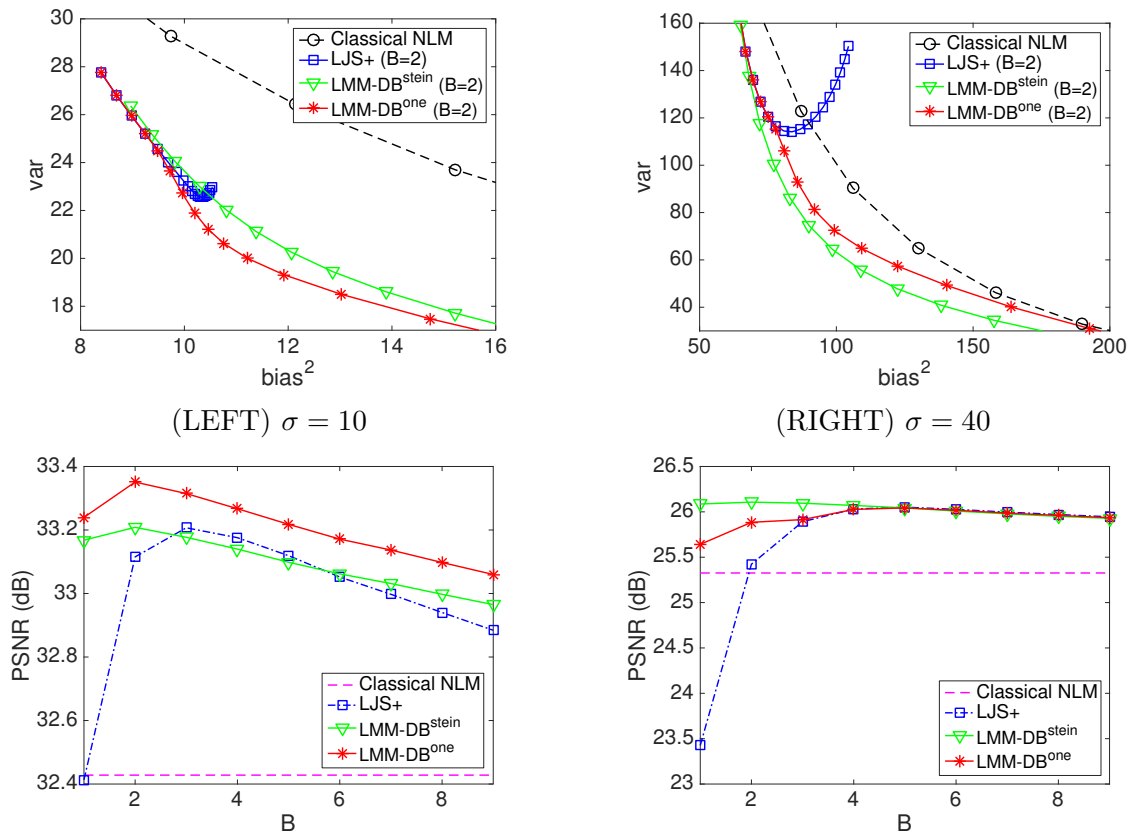
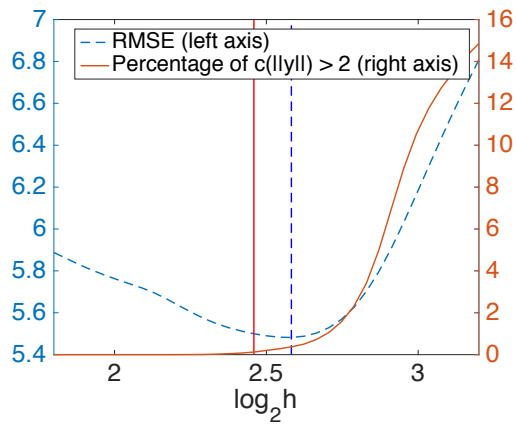
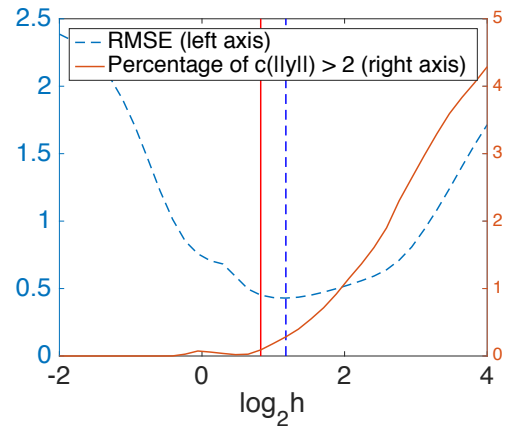


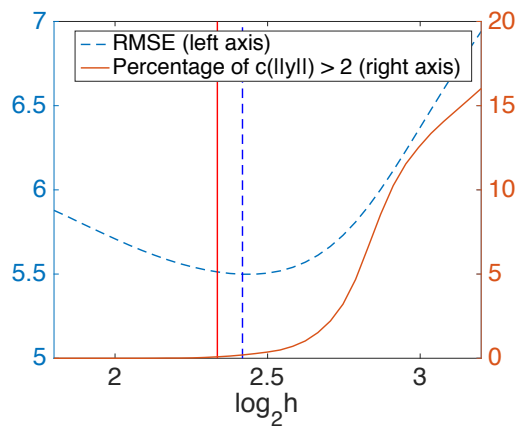
Figure 3.8: Bias-variance curves and PSNR over varying neighborhood size (B) using classical NLM (only in PSNR figure), LJS, and proposed LMM – DB^{stein} vs. LMM – DB^{one} for camera-man example.



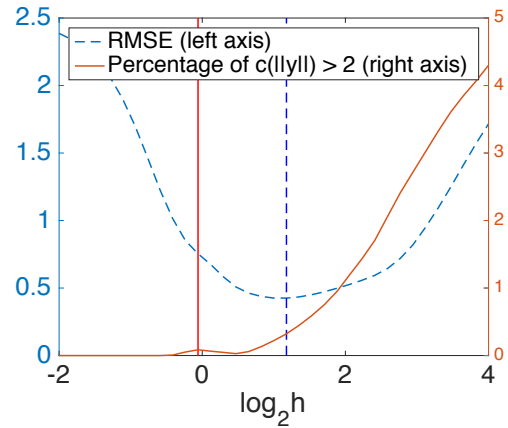
(a) cameraman LMM – DB^{one}



(b) SPECT LMM – DB^{one}



(c) cameraman LMM – RP^{one}



(d) SPECT LMM – RP^{one}

Figure 3.9: Comparison plots of RMSE vs. smoothing parameter h and the percentage of $c(\|s\|) > 2$ vs. the same smoothing parameter when using LMM-DB and LMM-RP with $B = 2$. $\sigma = 10$ for cameraman and $\sigma = 3$ for SPECT.

Table 3.3: PSNR values (dB) of proposed methods with $B = 2$ when choosing a smoothing parameter to yield the highest PSNR using the true image (TRUE) and when choosing a smoothing parameter to yield the percentage of $c(\|s\|) > 2$ to be 0.1% (ESTIMATED) for different noise levels.

	σ	LMM-DB ^{one}		LMM-RP ^{one}	
		TRUE	ESTIMATED	TRUE	ESTIMATED
<i>cameraman</i>	10	33.35	33.32	33.22	33.30
	20	29.47	29.47	29.30	29.45
	40	25.91	25.90	26.16	26.01
	60	23.43	23.43	23.78	23.60
<i>lena</i>	10	34.72	34.74	34.73	34.78
	20	31.22	31.20	31.47	31.37
	40	27.74	27.74	28.07	27.88
	60	25.60	25.63	25.95	25.82
<i>montage</i>	10	35.55	35.56	35.51	35.34
	20	31.24	31.20	31.33	31.32
	40	26.99	26.98	27.26	27.13
	60	24.07	23.97	24.54	24.16
<i>house</i>	10	35.32	35.35	35.30	35.37
	20	32.00	31.97	32.30	32.20
	40	27.82	27.79	28.35	28.06
	60	25.23	25.23	25.75	25.37
<i>pepper</i>	10	33.56	33.54	33.48	33.59
	20	29.81	29.80	29.91	29.95
	40	25.71	25.67	26.16	25.89
	60	23.15	23.02	23.81	23.24
<i>barbara</i>	10	33.67	33.68	33.62	33.73
	20	29.94	29.82	30.23	30.03
	40	25.79	25.69	26.47	25.92
	60	23.56	23.48	24.14	23.67
<i>boat</i>	10	32.80	32.80	32.73	32.79
	20	29.22	29.18	29.36	29.22
	40	25.44	25.60	25.99	25.75
	60	23.76	23.76	24.05	23.91
<i>hill</i>	10	32.66	32.64	32.60	32.61
	20	29.24	29.17	29.49	29.30
	40	26.01	25.99	26.38	26.05
	60	24.35	24.35	24.63	24.45
<i>couple</i>	10	32.82	32.80	32.79	32.81
	20	28.89	28.70	29.12	28.85
	40	25.08	25.05	25.52	25.10
	60	23.26	23.19	23.56	23.28
<i>fingerprint</i>	10	30.86	30.84	30.66	30.80
	20	27.07	26.86	27.05	26.96
	40	23.69	23.24	23.96	23.38
	60	21.47	20.77	21.92	21.02
<i>MRI</i>	10	40.83	40.83	40.77	40.90
	20	36.59	36.60	36.71	36.74
	40	32.36	32.36	32.58	32.56
	60	29.64	29.63	29.83	29.80
<i>SPECT</i>	3	55.44	55.04	55.55	50.58

CHAPTER IV

Conclusion

We proposed a joint spectral image reconstruction method to incorporate multiple energy windows in projector model and measurement data. Further evaluations of the proposed method will be performed with different energy ranges and widths for the acquisition windows. Comparison of the proposed method with [3, 28] will be performed in the near future. The proposed method was experimented only with Y-90, but could be applied to SPECT imaging of other radionuclide.

We also studied post-reconstruction NLM filter and proposed two methods (LMM-DB, LMM-RP) to determine self-weights of NLM filters that are “practically“ minimax. These methods yielded comparable PSNR, better bias-variance trade-offs, and reduced visual quality artifacts compared to the state-of-the-art LJS method over a wide range of natural images as well as SPECT images. Our methods also provide a potentially useful heuristic way of determining a global smoothing parameter without knowing the true image. Future works include studying noise properties and noise estimation techniques for SPECT, and investigate the proposed methods with the case of spatial variant noise.

References

- [1] Yuni K Dewaraja, Eric C Frey, George Sgouros, A Bertrand Brill, Peter Roberson, Pat B Zanzonico, and Michael Ljungberg, “Mird pamphlet no. 23: quantitative spect for patient-specific 3-dimensional dosimetry in internal radionuclide therapy,” *Journal of Nuclear Medicine*, vol. 53, no. 8, pp. 1310–1325, 2012. [iv](#), [4](#)
- [2] Yue Wu, Brian Tracey, Prem Natarajan, and Joseph P Noonan, “James-Stein type center pixel weights for non-local means image denoising,” *IEEE Signal Processing Letters*, vol. 20, no. 4, pp. 411–414, 2013. [v](#), [16](#), [17](#), [18](#), [19](#), [20](#), [21](#), [27](#), [28](#), [29](#), [31](#), [32](#), [33](#), [34](#)
- [3] Xing Rong, Yong Du, Michael Ljungberg, Erwann Rault, Stefaan Vandenberghe, and Eric C Frey, “Development and evaluation of an improved quantitative 90y bremsstrahlung spect method,” *Medical physics*, vol. 39, no. 5, pp. 2346–2358, 2012. [4](#), [8](#), [38](#)
- [4] Harrison H Barrett, Donald W Wilson, and Benjamin MW Tsui, “Noise properties of the em algorithm. i. theory,” *Physics in medicine and biology*, vol. 39, no. 5, pp. 833, 1994. [5](#)
- [5] Antoni Buades, Bartomeu Coll, and Jean-Michel Morel, “A review of image denoising algorithms, with a new one,” *Multiscale Modeling & Simulation*, vol. 4, no. 2, pp. 490–530, 2005. [6](#), [16](#), [17](#), [18](#), [22](#), [28](#), [30](#), [31](#)
- [6] Se Young Chun, Jeffrey A Fessler, and Yuni K Dewaraja, “Post-reconstruction non-local means filtering methods using CT side information for quantitative SPECT,” *Physics in Medicine and Biology*, vol. 58, no. 17, pp. 6225–6240, Aug. 2013. [6](#)

REFERENCES

- [7] C Kervrann and J Boulanger, “Optimal spatial adaptation for patch-based image denoising,” *IEEE Transactions on Image Processing*, vol. 15, no. 10, pp. 2866–2878, Sept. 2006. [6](#)
- [8] Tolga Tasdizen, “Principal components for non-local means image denoising,” in *15th IEEE International Conference on Image Processing (ICIP)*. IEEE, 2008, pp. 1728–1731. [6](#)
- [9] T Tasdizen, “Principal neighborhood dictionaries for nonlocal means image denoising,” *IEEE Transactions on Image Processing*, vol. 18, no. 12, pp. 2649–2660, Oct. 2009. [6](#)
- [10] P Coupe, P Yger, S Prima, P Hellier, C Kervrann, and C Barillot, “An optimized blockwise nonlocal means denoising filter for 3-D magnetic resonance images,” *IEEE Transactions on Medical Imaging*, vol. 27, no. 4, pp. 425–441, Apr. 2008. [6](#)
- [11] Zexuan Ji, Qiang Chen, Quan-Sen Sun, and De-Shen Xia, “A moment-based nonlocal-means algorithm for image denoising,” *Information Processing Letters*, vol. 109, no. 23, pp. 1238–1244, 2009. [6](#)
- [12] Sven Grewenig, Sebastian Zimmer, and Joachim Weickert, “Rotationally invariant similarity measures for nonlocal image denoising,” *Journal of Visual Communication and Image Representation*, vol. 22, no. 2, pp. 117–130, 2011. [6](#)
- [13] Ruomei Yan, Ling Shao, Sascha D Cvetković, and Jan Klijn, “Improved nonlocal means based on pre-classification and invariant block matching,” *Journal of Display Technology*, vol. 8, no. 4, pp. 212–218, 2012. [6](#)
- [14] Charles-Alban Deledalle, Vincent Duval, and Joseph Salmon, “Non-local methods with shape-adaptive patches (NLM-SAP),” *Journal of Mathematical Imaging and Vision*, vol. 43, no. 2, pp. 103–120, 2012. [6](#)
- [15] P Chatterjee and P Milanfar, “Patch-based near-optimal image denoising,” *IEEE Transactions on Image Processing*, vol. 21, no. 4, pp. 1635–1649, Mar. 2012. [6](#)
- [16] Chung Chan, Roger Fulton, Robert Barnett, David Dagan Feng, and Steven Meikle, “Postreconstruction nonlocal means filtering of whole-body PET with an anatomical prior,” *IEEE Transactions on Medical Imaging*, vol. 33, no. 3, pp. 636–650, Mar. 2014. [6](#)
- [17] Dimitri Van De Ville and Michel Kocher, “SURE-based non-local means,” *IEEE Signal Processing Letters*, vol. 16, no. 11, pp. 973–976, 2009. [6](#)

REFERENCES

- [18] Dimitri Van De Ville and M Kocher, “Nonlocal means with dimensionality reduction and SURE-based parameter selection,” *IEEE Transactions on Image Processing*, vol. 20, no. 9, pp. 2683–2690, Aug. 2011. [6](#)
- [19] Charles-Alban Deledalle, Florence Tupin, and Loïc Denis, “Poisson NL means: Unsupervised non local means for Poisson noise,” in *17th IEEE International Conference on Image Processing (ICIP)*. IEEE, 2010, pp. 801–804. [6](#)
- [20] Yue Wu, Brian H. Tracey, Premkumar Natarajan, and Joseph P Noonan, “Fast blockwise SURE shrinkage for image denoising,” *Signal Processing*, vol. 103, no. C, pp. 45–59, Oct. 2014. [6](#)
- [21] Bart Goossens, Quang Luong, Aleksandra Pizurica, and Wilfried Philips, “An improved non-local denoising algorithm,” in *International Workshop on Local and Non-Local Approximation in Image Processing*, Jaakko Astola, Karen Egiazarian, and Vladimir Katkovnik, Eds., Lausanne, Switzerland, 2008, pp. 143–156. [6](#)
- [22] Vincent Duval, Jean-François Aujol, and Yann Gousseau, “A bias-variance approach for the nonlocal means,” *SIAM Journal on Imaging Sciences*, vol. 4, no. 2, pp. 760–788, 2011. [6](#)
- [23] Charles Kervrann, Jérôme Boulanger, and Pierrick Coupé, “Bayesian non-local means filter, image redundancy and adaptive dictionaries for noise removal,” in *Scale Space and Variational Methods in Computer Vision*, pp. 520–532. Springer, 2007. [6](#)
- [24] Yue Wu, Brian Tracey, Prem Natarajan, and Joseph P Noonan, “Probabilistic non-local means,” *IEEE Signal Processing Letters*, vol. 20, no. 8, pp. 763–766, 2013. [6](#)
- [25] Alvin J Baranchik, “A family of minimax estimators of the mean of a multivariate normal distribution,” *The Annals of Mathematical Statistics*, vol. 41, no. 2, pp. 642–645, 1970. [7](#), [17](#), [20](#), [22](#), [23](#), [31](#)
- [26] David Minarik, K Sjögreen Gleisner, and Michael Ljungberg, “Evaluation of quantitative 90y spect based on experimental phantom studies,” *Physics in medicine and biology*, vol. 53, no. 20, pp. 5689, 2008. [8](#)
- [27] CF Unbe, PL Esquinas, H Piwowska-Bilska, D Pawlak, R Mikołajczak, B Birkenfeld, and A Celler, “Characteristics of brems strahlung emissions from radionuclide therapy isotopes,” in *Nuclear Science Symposium and Medical Imaging Conference (NSS/MIC), 2013 IEEE*. IEEE, 2013, pp. 1–3. [8](#)

REFERENCES

-
- [28] Mattijs Elschot, Marnix GEH Lam, Maurice AAJ van den Bosch, Max A Viergever, and Hugo WAM de Jong, “Quantitative monte carlo-based 90y spect reconstruction,” *Journal of Nuclear Medicine*, vol. 54, no. 9, pp. 1557–1563, 2013. [8](#), [38](#)
- [29] Se Young Chun and Jeffrey Fessler, “Noise properties of motion-compensated tomographic image reconstruction methods,” *Medical Imaging, IEEE Transactions on*, vol. 32, no. 2, pp. 141–152, 2013. [9](#)
- [30] Se Young Chun, Jeffrey Fessler, and Yuni K Dewaraja, “Correction for collimator-detector response in SPECT using point spread function template,” *Medical Imaging, IEEE Transactions on*, vol. 32, no. 2, pp. 295–305, 2013. [9](#)
- [31] Yuni K Dewaraja, Michael Ljungberg, and Jeffrey Fessler, “3-d monte carlo-based scatter compensation in quantitative i-131 spect reconstruction,” *Nuclear Science, IEEE Transactions on*, vol. 53, no. 1, pp. 181–188, 2006. [9](#)
- [32] Michael Ljungberg, Sven-Erik Strand, and Michael A King, *Monte Carlo calculations in nuclear medicine: Applications in diagnostic imaging*, CRC Press, 2012. [10](#)
- [33] WP Segars, G Sturgeon, S Mendonca, Jason Grimes, and Benjamin MW Tsui, “4d xcat phantom for multimodality imaging research,” *Medical physics*, vol. 37, no. 9, pp. 4902–4915, 2010. [10](#)
- [34] H Malcolm Hudson and Richard S Larkin, “Accelerated image reconstruction using ordered subsets of projection data,” *Medical Imaging, IEEE Transactions on*, vol. 13, no. 4, pp. 601–609, 1994. [10](#)
- [35] Vincent Doré and Mohamed Cheriet, “Robust NL-means filter with optimal pixel-wise smoothing parameter for statistical image denoising,” *IEEE Transactions on Signal Processing*, vol. 57, no. 5, pp. 1703–1716, 2009. [16](#), [18](#)
- [36] Thomas Brox and Daniel Cremers, “Iterated nonlocal means for texture restoration,” in *Scale Space and Variational Methods in Computer Vision*, pp. 13–24. Springer, 2007. [16](#)
- [37] Sebastian Zimmer, Stephan Didas, and Joachim Weickert, “A rotationally invariant block matching strategy improving image denoising with non-local means,” in *Proceedings International Workshop on Local and Non-Local Approximation in Image Processing*, 2008, pp. 135–142. [16](#)
- [38] Joseph Salmon, “On two parameters for denoising with non-local means,” *IEEE Signal Processing Letters*, vol. 17, no. 3, pp. 269–272, 2010. [16](#), [18](#), [22](#), [30](#)

REFERENCES

- [39] Charles Stein, “Inadmissibility of the usual estimator for the mean of a multivariate normal distribution,” in *Proceedings of the Third Berkeley symposium on mathematical statistics and probability*, 1956, vol. 1, pp. 197–206. [18](#), [20](#)
- [40] William James and Charles Stein, “Estimation with quadratic loss,” in *Proceedings of the fourth Berkeley symposium on mathematical statistics and probability*, 1961, vol. 1, pp. 361–379. [18](#), [20](#), [31](#)
- [41] Alvin John Baranchik, “Multiple Regression and Estimation of the Mean of a Multivariate Normal Distribution,” Tech. Rep. 51, Department of Statistics, Stanford University, May 1964. [20](#)
- [42] Bradley Efron and Carl Morris, “Families of minimax estimators of the mean of a multivariate normal distribution,” *The Annals of Statistics*, pp. 11–21, 1976. [20](#), [23](#)
- [43] William E Strawderman, “Proper Bayes minimax estimators of the multivariate normal mean vector for the case of common unknown variances,” *The Annals of Statistics*, pp. 1189–1194, 1973. [23](#)